Combining High Rate GPS and Strong Motion Data: A Kalman Filter Formulation for Real-Time Displacement Waveforms

Article · December 2010

3 authors:

Diego Melgar
University of California, Berkeley
108 PUBLICATIONS **3,131** CITATIONS

SEE PROFILE

Yehuda Bock
University of California, San Diego
273 PUBLICATIONS **15,913** CITATIONS

SEE PROFILE

Brendan W. Crowell
University of Washington Seattle
70 PUBLICATIONS **1,589** CITATIONS

SEE PROFILE

Some of the authors of this publication are also working on these related projects:

Project Dynamic Strains for Earthquake Source Characterization View project

Project Stochastic fault patterns: Illuminating the rupture complexity of historical tsunamigenic earthquakes in the South American subduction zone (15°S to 30°S) View project

Real-Time Strong-Motion Broadband Displacements from Collocated GPS and Accelerometers

by Yehuda Bock, Diego Melgar, and Brendan W. Crowell

Abstract   We present a new solution to the classical problem of deriving displacements from seismic data that is suitable for real-time monitoring. It relies on an optimal combination of collocated high-rate GPS displacements and very high-rate strong-motion accelerometer data using a Kalman filter that takes advantage of the individual strengths of seismic and geodetic networks while minimizing their weaknesses. The result is a more accurate broadband estimate of velocities and displacements at the higher rate provided by accelerometers. In contrast to displacements inferred through integration of seismic data alone, which are degraded by the presence of unphysical drifts and limited dynamic ranges, broadband displacements do not drift and will not clip. Furthermore, they are more accurate and robust than those obtained solely from GPS receivers. We establish the accuracy and precision of the new solution using earthquake engineering data from the University of California, San Diego's Large High-Performance Outdoor Shake Table. Then we estimate broadband displacements for the 2010 M_w 7.2 El Mayor–Cucapah earthquake using 1 Hz GPS displacements and 100 Hz accelerometer data from collocated sensors in southern California. We also reconstruct velocity measurements equivalent to those of broadband seismometers, which clipped at stations hundreds of kilometers from the epicenter during the earthquake. The ability to obtain broadband displacement waveforms in three dimensions with millimeter precision is a breakthrough for a number of areas ranging from earthquake source physics to the response of long-period engineered structures. To do so in real time from a dense monitoring network provides distinct advantages for earthquake early warning and rapid earthquake response.

Introduction

Dense space geodetic networks of continuous Global Positioning System (CGPS) instruments built over the last two decades to monitor crustal deformation are now considered an integral part of earthquake science infrastructure, on par with seismic networks. Although the observational goal of both geodetic networks and seismic networks is ground displacement, they have developed for the most part independently, with the former deployed to measure long-period static deformation and the latter to measure dynamic motions. Hence, seismic networks have been designed to acquire low-latency, very high-rate observations by seismometers and accelerometers, while geodetic networks have only required the accumulation of low-rate (15–30 s) satellite observations over days to hours (high latency) by GPS instruments. In the last decade it has been demonstrated that geodetic networks can also be used to directly measure dynamic ground displacements generated by medium to large earthquakes ("GPS seismology", Nikolaidis *et al.*, 2001; Larson *et al.*, 2003; Hammond *et al.*, 2010). Furthermore, they measure coseismic and postseismic displacements and other transient

motion whether or not these are accompanied by seismic shaking. The value of geodetically determined static displacements is now well established: they provide important constraints on earthquake faulting, including the location and extent of the rupture plane, unambiguous resolution of the nodal plane, and the distribution of slip on the fault unbiased by rupture velocity assumptions

With seismic data, displacements are obtained by a single integration of observed broadband velocities or a double integration of observed accelerations. Velocity measurements are preferred because the conversion to displacement requires one less integration. Due to the dynamic range limits of seismometers the accuracy of absolute displacements so derived is poor. With geodetic data, observations of phase and pseudorange measurements to all visible GPS satellites are converted to positions using one of several geodetic analysis methodologies. Displacements are then derived from changes in position over time. Seismic measurements are local and quantified with respect to an inertial frame. Although the GPS antenna needs to be aligned with the local

vertical and gravity field, GPS instruments provide spatial (noninertial) observations with respect to a global terrestrial reference frame.

Although broadband seismometers and strong-motion accelerometers are many orders of magnitude more sensitive to dynamic displacements, at low frequencies (less than 1 Hz), GPS noise levels roughly agree with the upper limit of the dynamic range of broadband seismic sensors (Genrich and Bock, 2006). Together, GPS and broadband seismic sensors cover the entire possible range of seismic surface displacement at frequencies less than 1 Hz. For adequate coverage at the higher frequencies and for strong-motion scenarios when broadband seismometers can clip, seismic stations are augmented by accelerometers. Modern, geodetic-grade GPS receivers can also be used to estimate higher frequency displacements (at 10–50 Hz sampling rates) with a comparable precision to that of 1 Hz samples (Genrich and Bock, 2006). However, accelerometers have the advantage that they are more sensitive to ground motions than GPS instruments, and more so in the vertical direction where measurement of single-epoch high-rate GPS displacements is about an order of magnitude less precise than in the horizontal (e.g., Bock *et al.*, 2000). Also, accelerometer data are much less verbose than raw GPS data, which becomes a practical issue in terms of telemetry requirements at very high sampling rates. On the other hand, the double integration from acceleration observations to displacements is problematic and accompanied by unphysical drifts due to sensor rotation and tilt, hysteresis, and imprecision in the numerical integration process (Boore, 2001), while GPS displacements are estimated directly. Nikolaidis *et al.* (2001) demonstrated that GPS displacements can serve as long-period constraints for the deconvolution of accelerometer data, using data collected at Piñon Flat Observatory during the 1999 M_w 7.1 Hector Mine earthquake. By using the estimated GPS static offset, they were able to recover a more accurate record of the ground displacement compared with the displacement signal from either of the individual sensors. Emore *et al.* (2007) used a constrained inversion technique to combine GPS displacements and accelerometer data from the 2003 M_w 8.3 Tokachi-oki earthquake to estimate displacements and step function offsets in accelerometer records, after correcting for possible misorientation of the accelerometers.

Here we present a new methodology to optimally estimate very high-rate displacements in real time (within a few seconds) from a combination of high-rate GPS displacements and very high-rate raw accelerometer data using a Kalman filter, which preserves the best and avoids the worst characteristics of each. Our approach is a less subjective and more accurate method to integrate accelerometer data that avoids problematic baseline corrections and results in an improved broadband record of ground displacements, that is, which spans the broadest possible spectrum of dynamic motion including the static deformation. Because this approach is not of widespread use in seismology, an overview of the basic concepts and a description of the Kalman filter and smoother are presented. Throughout, we use the term "broadband displacements" to denote the total of both static and dynamic displacements, either through analysis of GPS data alone or combined analysis of GPS-derived displacements and accelerometer data.

Several studies have used independently derived seismic and high-rate GPS displacements to model the earthquake source well after the fact (e.g., Ji *et al.*, 2004; Rolandone *et al.*, 2006; Kim and Dreger, 2008). However, combining GPS and accelerometer data at the observational level to estimate improved very high-rate broadband displacements prior to the modeling phase provides benefits in subjects ranging from earthquake source physics to the response of long-period engineered structures. To date, full waveform inversions are only performed using seismic data, and none use displacement directly. They suffer from the inability to obtain the static offset associated with a large earthquake, and usually underestimate fault slip. As a result they rely on a rupture model to infer the seismic moment of the earthquake from the observed seismic record from which a moment magnitude is derived. For large events, the methodology used to derive a centroid moment tensor (CMT) tends to underestimate the full seismic moment release (Kedar *et al.*, 1994; Park *et al.*, 2005). Broadband displacement waveforms described here can be used to better determine time-dependent slip distribution and moment tensor solutions along fault surfaces after large earthquakes.

Being specifically designed for real-time monitoring, our method provides distinct advantages for rapid earthquake response, for example, in determining the magnitude of a large earthquake more quickly or deciding whether the rupture will propagate over part of or the entire fault. Earthquake early warning systems (Gasparini *et al.*, 2007; Allen *et al.*, 2009, Astiz, 2009) have relied solely on seismic measurements, although most algorithms use displacement when trying to estimate the potential magnitude of an event from the initial few seconds. Estimates of magnitude are made on the ratio of the short-term average displacement to the long-term average and on the apparent frequency of the first arrivals of body waves. This concept has been further developed using the *W*-phase, a long-period phase arriving between the *P* and *S* wave (Kanamori and Rivera, 2008), to provide rapid moment tensor solutions at regional and teleseismic distances. Probabilistic approaches have been used to infer whether an earthquake rupture will continue or stop based upon the seismic records to that point (e.g., Böse and Heaton, 2010). These and other algorithms would benefit from the ability to provide real-time access to broadband displacements closer to the source, especially for larger earthquakes. The goal is rapid detection followed by prediction of the resulting strong ground shaking for the purpose of warning those in harm's way (e.g., Heaton, 1985).

It is clear that geodetic and seismic networks are complementary in terms of spanning the broadest possible frequency range of surface displacement, including dynamic and static components. Considering their history of development,

as well as the different siting requirements for seismometers and GPS instruments, it is not surprising that there are very few station collocations. We demonstrate in this paper that collocation of GPS and seismic sensors provides distinct advantages and should be given a high priority.

Estimation of GPS Displacements

In this section, we provide an overview of GPS positioning techniques in the context of current real-time capabilities and describe how GPS displacements are derived with respect to a local reference frame. The motivation is to be able to unambiguously compare GPS-derived and seismically derived displacements, and to optimally combine GPS displacements and accelerometer data to estimate broadband displacement waveforms.

Overview of GPS Positioning

There are two basic approaches to precise GPS data analysis: network positioning and precise point positioning. In both approaches station positions are estimated with respect to a global Cartesian terrestrial reference system. This system is realized by the published coordinates and velocities of hundreds of global geodetic stations in the International Terrestrial Reference Frame (ITRF), the latest version being ITRF2008 (see Data and Resources). Precise GPS satellite orbital products distributed by the International GNSS Service (IGS; see Data and Resources) are tied to this underlying reference frame, and without loss of generality, are assumed to be fixed in the GPS data analysis.

In network positioning, data from a network of stations are analyzed simultaneously to estimate station positions and integer-cycle phase ambiguities (e.g., Dong and Bock, 1989; Blewitt, 1989) and other parameters such as zenith troposphere delays. Analyzing the data as a network results in the effective cancellation of GPS receiver clock and satellite clock errors, which are common to multiple satellites and stations, respectively. Precise point positioning (Zumberge et al., 1997) relies on fixed satellite orbits, as well as satellite clock parameters also available through the IGS and/or its different analysis centers (Kouba and Heroux, 2001). These parameters are held fixed in the process of estimating ITRF positions of individual CGPS stations, phase ambiguities, zenith troposphere delays, and station clock parameters.

Network positioning and precise point positioning approaches can be considered equivalent, in terms of the underlying physics. However, to achieve geodetic-quality positions (mm- to cm-level), it is essential to resolve integer-cycle phase ambiguities to their correct integer values (Blewitt, 1989; Dong and Bock, 1989). This is straightforward for batch postprocessing, which includes the simultaneous analysis of multiple GPS data records, usually sampled at rates of 15–30 s, to derive a single station position over the entire sampled interval. It is the source of the typical 24-hour GPS position time series used to study permanent

deformation, including long-term tectonic motion, as well as coseismic, postseismic and other transient deformation (Fig. 1). Batch postprocessing plays a role in seismological applications by providing highly accurate, true-of-date ITRF station positions with respect to which displacement waveforms can be estimated during an event. There are several analysis groups that are producing 24-hour position time series on an operational basis (see Data and Resources).

Of primary importance in seismological applications is the estimation of centimeter-level or better displacements at the GPS receiver sampling rate, typically 1 Hz. Postprocessed single-epoch network positioning with resolution of integer-cycle phase ambiguities is now routinely applied to GPS seismology (e.g., Larson et al., 2003; Bock et al., 2004; Miyazaki et al., 2004; Ji et al., 2004; Prawirodirdjo et al., 2010), tsunami warning (e.g., Blewitt et al., 2006; Blewitt et al., 2009), and volcano monitoring (e.g., Cervelli et al., 2006). However, a general real-time solution is still elusive, and analysis of multiple data epochs is usually required to resolve integer-cycle phase ambiguities and estimate single-epoch positions.

Precise point positioning has been limited in GPS seismology, in particular for real-time applications, because of unresolved integer-cycle phase ambiguities and slow convergence rates and reconvergence rates when loss of lock on the satellite signals occurs. JPL's Global Differential GPS System (GDGPS) employs a large global ground network of real-time reference receivers and real-time data processing software, which allows a single GPS receiver to be point positioned with 10–20 cm accuracy anywhere in the world. This level of accuracy is considered useful for global tsunami warnings generated by great earthquakes (Bar-Sever et al., 2009). A relatively new area of geodetic research is rapid integer-cycle ambiguity resolution in precise point positioning without the need for specific reference stations. Besides fixed satellite orbits and clocks, and estimation of positions, receiver clocks and tropospheric delays of the GPS signals, it also requires prediction of ionospheric delays. Recent results have been encouraging in that reliable ambiguity resolution and centimeter-level positioning accuracies have been achieved with only a few epochs of 1 Hz GPS data for reconvergence, although about a 20-min convergence period is still required (e.g., Geng, 2010).

Real-Time Instantaneous Positioning

Here we apply the method of instantaneous GPS positioning (Bock et al., 2000) to estimate displacement waveforms in real time. This approach provides real-time position estimates at the receiver sampling rate, through network-based, single-epoch resolution of integer-cycle phase ambiguities. This approach has been successfully applied to GPS seismology (Nikolaidis et al., 2001; Bock et al., 2004), volcano monitoring (Mattia et al., 2004), structural monitoring (Kogan et al., 2008), ice shelf rift propagation (Bassis et al., 2007), and earthquake early warning (Crowell et al., 2009).

Langbein and Bock (2004) reported 6 mm horizontal precision at the 99% confidence level for a few seconds to a few hours of 1 Hz GPS displacements, with an order of magnitude less precision in the vertical.

Typically, and for computational efficiency, the larger network is divided into multiple subnetworks with a two-station overlap between adjacent subnetworks; positions are estimated relative to the true-of-date ITRF coordinates of an arbitrary station within each subnetwork. Then a network adjustment is performed to estimate coordinates for all stations with respect to the true-of-date ITRF coordinates of one or more stations outside the zone of deformation (Crowell et al., 2009). Displacements are then the result of the changing single-epoch positions with respect to their true-of-data ITRF coordinates just prior to the onset of deformation, determined with millimeter accuracy through extrapolation of a 24-hour time series (Fig. 1).

The single-epoch subnetwork analysis includes estimation of station positions relative to the fixed true-of-date ITRF coordinates of an arbitrary station within the subnetwork, zenith tropospheric delays for each station, and integer-cycle phase ambiguities. Predicted satellite orbital positions (ephemeris) provided by the IGS are held fixed and, if available, troposphere models (e.g., Gutman, 2008) are used to constrain the tropospheric delay parameters. The maximum effective intersite spacing within each subnetwork for robust single-epoch resolution of integer-cycle phase ambiguities is a function of the magnitude of atmospheric errors, in particular the level of ionosphere variation across each subnetwork

(e.g., Bock et al., 2000). For GPS seismology, instantaneous positioning has been effective in real-time analysis of medium to large earthquakes within dense geodetic networks of large extent with station spacing of ∼20–40 km. Examples include the 2003 M_w 8.3 Tokachi-oki earthquake (Crowell et al., 2009) using 1 Hz GeoNet data in Japan (Miyazaki et al., 1998), and as described in this paper the 2010 M_w 7.2 El Mayor–Cucapah earthquake using 1 Hz data from the California Real-Time Network (CRTN; Genrich and Bock, 2006) and the Plate Boundary Observatory (PBO—Jackson, 2003). To aid in resolution of phase ambiguities, a differential ionospheric constraint (Schaffrin and Bock, 1988; Bock et al., 2000) is applied, and the relative station positions within each subnetwork are constrained to a level that is unlikely to be exceeded in a large earthquake (∼1 m). For example, the maximum relative motion encountered between adjacent stations closest to the epicenter of the El Mayor–Cucapah earthquake was 0.58 m for stations located less than 20 km apart.

At each epoch and prior to the network adjustment step it is necessary to ascertain which parts of the overall network are being displaced so that an appropriate reference station can be selected. This can be done on-the-fly by examining each subnetwork for internal deformation. The selection of the reference station is important, but as long as the station is sufficiently far away (typically, several hundreds of kilometers), has a good station history (i.e., stability of monument, no latency, and no data completeness issues), and is contained within a subnetwork that has relatively short
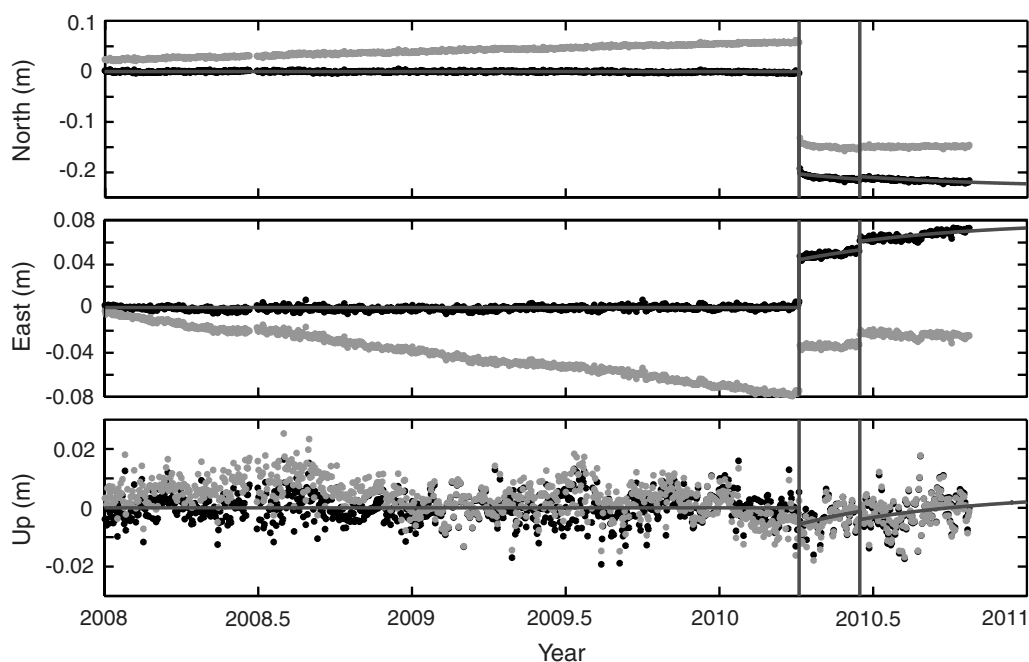

Figure 1. Typical daily coordinate time series at station P494 (32º.7597 N, 115º.7321 W) in southern California in local (N, E, U) frame, after transformation from ITRF2005 global Cartesian (X, Y, Z) coordinates using equation (1). The raw daily solution time series are in gray, while the ones in black have had the long-term plate rate and the annual and semiannual terms removed. The two vertical lines indicate static offsets from the 4 April 2010 M_w 7.2 El Mayor–Cucapah earthquake and an M_w 5.8 aftershock on 15 June 2010 (UTC). The model fit to the time series (gray line) includes postseismic relaxation with an exponential decay and a time constant of 0.47 years.

baselines, it will serve to track the strongest ground motions closest to the hypocenter. For real-time integration, a list of good candidate reference stations could be prepared from which a reference station could be selected based on its distance to the hypocenter. Usually, the fixed site position is constant throughout the entire network adjustment, but this is not a requirement. It does, however, propagate any dynamic motions at the fixed station throughout the network, but if one chooses a station several hundred kilometers away from an event, this effect should be minimal. It may be possible to use positions computed through rapid precise point positioning or to use an iterative approach.

Displacements in a Local Reference Frame

Without loss of generality or consideration for the particular GPS analysis technique used, or whether or not it is performed in real time or postprocessing, we assume that displacement waveforms are available for a geophysical event (e.g., earthquake) for one of more CGPS stations with centimeter-level or better single-epoch precision at, for example, the typical 1 Hz sampling rate of current real-time geodetic networks. Consider that we know the precise coordinates (X_0, Y_0, Z_0) of a CGPS station in a global Cartesian reference frame (e.g., ITRF2005) just prior to an earthquake, at time t_0. The prior coordinates represent true-of-date values. The station is then subjected to a combination of dynamic and static displacements. The subsequent coordinates of the station are denoted by (X_i, Y_i, Z_i), where i denotes the i'th epoch after the event. The displacement at the i'th epoch can be simply computed (as $X_i - X_0$, $Y_i - Y_0$, $Z_i - Z_0$). In order to compare the geodetic displacements with displacements derived from a single integration of broadband seismic velocities or a double integration of accelerations, we need to transform the displacements from a (right-handed) global Cartesian frame (X, Y, Z) into a (left-handed) local north, east, up frame (N, E, U) by the following transformation

$$
\begin{bmatrix} \Delta N_i \\ \Delta E_i \\ \Delta U_i \end{bmatrix} = \begin{bmatrix} 1 & 0 & 0 \\ 0 & 1 & 0 \\ 0 & 0 & -1 \end{bmatrix} \boldsymbol{R}_2\left(\frac{3\pi}{2} - \varphi\right) \boldsymbol{R}_3(\lambda) \begin{bmatrix} X_i - X_0 \\ Y_i - Y_0 \\ Z_i - Z_0 \end{bmatrix}
$$

$$
= \begin{bmatrix} -\sin\phi\cos\lambda & -\sin\lambda\sin\phi & \cos\phi \\ -\sin\lambda & \cos\lambda & 0 \\ \cos\lambda\cos\phi & \cos\phi\sin\lambda & \sin\phi \end{bmatrix}
$$

$$
\times \begin{bmatrix} X_i - X_0 \\ Y_i - Y_0 \\ Z_i - Z_0 \end{bmatrix}, \tag{1}
$$

where $\boldsymbol{R}_2$ and $\boldsymbol{R}_3$ are rotation matrices around the Y and Z axes, respectively, and (ϕ, λ) is the geodetic latitude and longitude of the station. The geodetic displacements in the (N, E, U) frame can then be compared directly with local displacements derived through single integration of seismometer data or double integration of accelerometer data.

Broadband Displacements Using a Kalman Filter

In current seismological practice, strong-motion displacements are obtained from double integration of accelerometer data. Using high-dynamic-range broadband acceleration recordings, it is possible to retrieve displacement waveforms that include the permanent static deformation. There are, however, multiple difficulties in this procedure: displacement waveforms obtained in this manner show unphysical drift due to sensor rotation and tilt (Trifunac and Todorovska, 2001; Lee and Trifunac, 2009), hysteresis (Shakal and Petersen, 2001), and to a lesser degree, imprecision in the numerical integration process (Boore et al., 2002; Smyth and Wu, 2006). These problems are generally accounted for by either high-pass filtering or function fitting of the velocity time series obtained after a single integration (Graizer, 1979; Iwan et al., 1985; Boore, 2001; Boore et al., 2002). Function fitting is more desirable than high-pass filtering because it retains the static offset. If the parameters of the fitted function are properly selected, then the resulting displacements are considered broadband, that is, the derived displacements are accurate records of the dynamic shaking at a wide range of frequencies, including the static (DC) offset. As Boore et al. (2002) point out, however, this scheme suffers from the fact that there is no objective way of selecting the parameters of the function to be fit and multiple functions can yield seemingly plausible waveforms. Without extra geodetic information such as InSAR or GPS to constrain the static offset, it is up to each researcher to select these parameters based on what looks best. Additionally, the function parameters for correction vary for each station and for each event, making it impractical to implement such a scheme in real time for hazards applications such as early warning systems or across a large network.

We present a less subjective and more accurate approach to the integration of accelerometer data that avoids problematic baseline corrections or function form fitting and results in an improved broadband record of ground displacements, that is, which spans the broadest possible spectrum of dynamic motion including the static deformation. Using a Kalman filter, we optimally combine raw very high-rate (e.g., 100 Hz) accelerations with high-rate (e.g., 1 Hz) displacements derived from collocated GPS receivers to estimate very high-rate displacements. This approach is suitable for dense networks and real-time processing required by early warning systems and rapid earthquake response. Furthermore, it is more robust and accurate than GPS-only solutions. This is a novel approach in seismology, so an overview of the basic concepts and a derivation of the appropriate filters are in order. This is by no means a comprehensive review as important results have been proved elsewhere, and interested readers are directed to the cited references. A multirate Kalman filter was proposed for structural engineering applications by

Smyth and Wu (2006) and applied to bridge monitoring by Kogan *et al.* (2008).

The Kalman Filter

In the theory of control and estimation, the problem of extracting, separating, or detecting a random signal in the presence of noise is known as the Wiener problem. Kalman filters are a solution to this problem using the state-space representation of dynamical systems (Kalman, 1960). A dynamical system can be characterized by its state. The state can be understood as all the information about the past behavior of the system necessary to predict its future behavior. The dynamics of the system are then described by state transitions. There is abundant engineering literature on the subject of state-space description of dynamical systems. For the basic filter formulation we follow Maybeck (1970), who shows that a discrete dynamical system can be described by

$$\mathbf{x}_{k+1} = \mathbf{A}_k\mathbf{x}_k + \mathbf{B}_k\mathbf{u}_k + \mathbf{G}_k\boldsymbol{\alpha}_k, \tag{2}$$

where $\mathbf{x}$ is the state n-vector whose components are the state variables (note that the subindex indicates a progression in time, not a component of the vector), $\mathbf{A}$ is an $n \times n$ matrix describing the system dynamics (the physics governing the system), $\mathbf{u}$ is an m-vector describing the system inputs (in our application, raw accelerometer data), $\mathbf{B}$ is an $n \times m$ input matrix, $\boldsymbol{\alpha}$ is an l-vector of system noise with distribution $\boldsymbol{\alpha} \sim (\mathbf{0}, \mathbf{Q})$ (zero mean and covariance matrix $\mathbf{Q}$), and $\mathbf{G}$ is an $n \times l$ noise input matrix. The presence of the subindex k on all terms of the equation indicates that in its most general form the description presented here allows for a system that changes its properties at every timestep.

Additionally, measurements of the system may be available at discrete time intervals; these can be expressed by a linearized model

$$\mathbf{z}_k = \mathbf{H}_k\mathbf{x}_k + \boldsymbol{\beta}_k, \tag{3}$$

where $\mathbf{z}$ is a p-vector of measurements (in our application, GPS displacements), $\mathbf{H}$ is a $p \times n$ design matrix, and $\boldsymbol{\beta}$ is a p-vector measurement noise with a distribution $\boldsymbol{\beta} \sim (\mathbf{0}, \mathbf{R})$ (zero mean and covariance matrix $\mathbf{R}$). It is assumed that the vectors $\boldsymbol{\alpha}$ and $\boldsymbol{\beta}$ are uncorrelated. It will also be convenient and physically reasonable when applied to seismology to assume that the system and measurements noise vectors have white (Gaussian) distributions, although this is not necessary in the generalized Kalman filter formulation.

The Kalman filter operates using a Bayesian estimation approach. It propagates the conditional probability densities, that is, the probability that the system states have a certain value given the measurements up to a given instant. In this sense the Kalman filter is an optimal estimator of the system states where by optimality we mean a minimum error unbiased estimator (Maybeck, 1970). The filter is a recursive algorithm that utilizes data on a sample by sample basis rather than a batch algorithm that incorporates all the information simultaneously. It operates on linear systems,

although it is possible to apply it to nonlinear systems by the extended Kalman filter (Chui and Chen, 2009), and as such combines the measurements with the information known from the system model to provide state estimates in a two stage process.

Following Maybeck (1970) if the state covariance matrix is $\mathbf{P}$ then after initializing the state vector and the state covariance matrix, the next step, known as time update, is to obtain the *a priori* state covariance matrix from

$$\mathbf{P}_{k+1}^- = \mathbf{A}_k\mathbf{P}_k\mathbf{A}_k^T + \mathbf{G}_k\mathbf{Q}_k\mathbf{G}_k^T, \tag{4}$$

and the *a priori* state estimate from

$$\hat{\mathbf{x}}_{k+1}^- = \mathbf{A}_k\hat{\mathbf{x}}_k + \mathbf{B}_k\mathbf{u}_k. \tag{5}$$

The hat notation $\hat{\mathbf{x}}$ indicates the obtained quantity is an estimate, and the super index $\mathbf{P}^-$ indicates a quantity obtained before the measurement process. The second step is to incorporate the measurements into the measurement update or innovation phase by computing the *a posteriori* state covariance as

$$\mathbf{P}_{k+1} = [(\mathbf{P}_{k+1}^-)^{-1} + \mathbf{H}_{k+1}^T\mathbf{R}_{k+1}^{-1}\mathbf{H}_{k+1}]^{-1}, \tag{6}$$

and the *a posteriori* state estimate as

$$\begin{aligned}\hat{\mathbf{x}}_{k+1} &= \hat{\mathbf{x}}_{k+1}^- + \mathbf{P}_{k+1}\mathbf{H}_{k+1}^T\mathbf{R}_{k+1}^{-1}(\mathbf{z}_{k+1} - \mathbf{H}_{k+1}\hat{\mathbf{x}}_{k+1}^-) \\ &= \hat{\mathbf{x}}_{k+1}^- + \mathbf{K}_{k+1}(\mathbf{z}_{k+1} - \mathbf{H}_{k+1}\hat{\mathbf{x}}_{k+1}^-),\end{aligned} \tag{7}$$

where the matrix $\mathbf{K}$ is known as the Kalman gain. In a sense the Kalman gain weights the adjustment to the *a priori* estimate once a measurement is available by modulating the correction to be applied due to the measurement residual, $\mathbf{z}_{k+1} - \mathbf{H}_{k+1}\hat{\mathbf{x}}_{k+1}$, which is the difference between the *a priori* state estimate and the actual measurement.

One caveat is that the system we will analyze (ground displacement) is not discrete by nature as in the formulation shown previously and as we shall see discretizing the system affects some of the state matrices. Lewis *et al.* (2008) showed that a continuous system analogous to equation (2) can be written as

$$\dot{\mathbf{x}}(t) = \mathbf{A}\mathbf{x}(t) + \mathbf{B}\mathbf{u}(t) + \mathbf{G}\boldsymbol{\alpha}(t), \tag{8}$$

with measurements

$$\mathbf{z}(t) = \mathbf{H}\mathbf{x}(t) + \boldsymbol{\beta}(t),$$

where, as before, $\boldsymbol{\alpha} \sim (\mathbf{0}, \mathbf{Q})$ and $\boldsymbol{\beta} \sim (\mathbf{0}, \mathbf{R})$ and $\boldsymbol{\alpha}$ and $\boldsymbol{\beta}$ are white noise processes uncorrelated with each other. After some manipulation the system can be transformed to the discrete form

$$\mathbf{x}_{k+1} = \mathbf{A}^s\mathbf{x}_k + \mathbf{B}^s\mathbf{u}_k + \boldsymbol{\alpha}_k, \tag{10}$$

and the measurement process

$$z_k = H_k x_k + \beta_k, \qquad (11)$$

where now we have $\alpha(t) \sim (0, Q^s)$ and $\beta(t) \sim (0, R^s)$, the superscript s indicates the discretized or sampled version of the continuous matrices. Notice that H is unaltered by the sampling process. Lewis *et al.* (2008) also show that if the sampling interval is τ, then one can write the sampled matrices as

$$A^s = e^{A\tau} = I + A\tau + \frac{A^2\tau^2}{2!} + \cdots, \qquad (12)$$

$$B^s = \int_0^\tau e^{A\tau} B \, dt = B\tau + \frac{AB\tau^2}{2!} + \cdots, \qquad (13)$$

$$Q^s = \int_0^\tau e^{A\tau} GQG^T e^{A^T\tau} dt$$
$$= GQG^T\tau + \frac{(AGQG^T + GQGA^T)\tau^2}{2!} + \cdots, \quad (14)$$

and

$$R^s = \frac{R}{\tau}. \qquad (15)$$

The series expansions are used in truncated form for numerical computation.

Fusing GPS and Strong-Motion Accelerometer Data

Now to apply this to the problem at hand, the estimation of ground displacements at an observing station, we can assume one-dimensional motion and formulate the problem independently for each coordinate (N,E,U) direction as a first-order linear differential equation using the continuous state-space representation (8) as

$$\dot{x}_k = \begin{bmatrix} 0 & 1 \\ 0 & 0 \end{bmatrix} x + \begin{bmatrix} 0 \\ 1 \end{bmatrix} a_k + \begin{bmatrix} 0 \\ 1 \end{bmatrix} \alpha_k, \qquad (16)$$

where the state vector comprises the displacement d_k and velocity v_k,

$$x_k = \begin{bmatrix} d_k \\ v_k \end{bmatrix}. \qquad (17)$$

The assumption is that the acceleration a_k driving the system (the input) is constant in between time steps, with α_k as the system noise. Applying (12)–(15) to discretize (16) and letting

$$Q = \begin{bmatrix} 0 & 0 \\ 0 & q \end{bmatrix}, \qquad (18)$$

because the only source of noise is in the input accelerations, the elements for the discrete system model (10) are given by

$$A^s = \begin{bmatrix} 1 & \tau_a \\ 0 & 1 \end{bmatrix}; \qquad B^s = \begin{bmatrix} \tau_a^2/2 \\ \tau_a \end{bmatrix};$$

$$Q^s = \begin{bmatrix} q\tau_a^3/3 & q\tau_a^2/2 \\ q\tau_a^2/2 & q\tau_a \end{bmatrix}; \qquad R^s = \frac{r}{\tau_d}, \qquad (19)$$

where τ_a and τ_d are the accelerometer and GPS sampling intervals, respectively, q is the acceleration variance, and r is the measurement noise variance. Notice that because $G = I$, there is no need to discretize G. Finally, the measurement process for the GPS displacements in each coordinate direction is given by

$$z_k = \begin{bmatrix} 1 & 0 \end{bmatrix} \begin{bmatrix} d_k \\ 0 \end{bmatrix} + \beta_k, \qquad (20)$$

where $\beta_k \sim (0, r)$ is the GPS displacement noise.

Using the elements of the discrete state equations (10) provided by (19) and with measurement process (20), the forward Kalman filter algorithm for fusing GPS and accelerometer data can be used to determine the state variables, displacement and velocity at each time step and in each coordinate direction as follows:

• Initialization: $x_0 = 0$; $P_0 = I$
• Time update (*a priori* estimate)

$$P_{k+1}^- = A_k P_k A_k^T + Q_k, \qquad (21)$$

$$\hat{x}_{k+1}^- = A_k \hat{x}_k + B_k u_k. \qquad (22)$$

• Measurement update (*a posteriori* estimate)

$$P_{k+1} = [(P_{k+1}^-)^{-1} + H_{k+1}^T R_{k+1}^{-1} H_{k+1}]^{-1}, \qquad (23)$$

$$\hat{x}_{k+1} = \hat{x}_{k+1}^- + P_{k+1} H_{k+1}^T R_{k+1}^{-1} (z_{k+1} - H_{k+1} \hat{x}_{k+1}^-). \quad (24)$$

The accelerometer time series at sampling interval τ_a provides the system input, while the GPS displacements at sampling interval τ_d feed the measurement process. GPS sampling frequencies are traditionally lower (1–5 Hz) than strong-motion accelerometer sampling frequencies (80–250 Hz), thus the formulation needs to be adapted to this multirate environment (Smyth and Wu, 2006) by performing the time update stage in equations (21) and (22) at every timestep and applying the measurement update stage in equations (23) and (24) only when a GPS sample becomes available (in the absence of measurements there is zero Kalman gain). For algorithmic simplicity it is useful if the sampling frequency of the strong-motion accelerometer is a multiple of GPS sampling frequency. In this way the measurement update can be done at regular intervals, but this is not a requirement.

Also if the sampling frequencies remain constant throughout and the noise characteristics do not change, then $\mathbf{A}^s$, $\mathbf{B}^s$, $\mathbf{Q}^s$, and $\mathbf{R}^s$ in equation (19) remain unchanged. However, the sampling frequencies for both instruments can vary throughout the filtering process as long as the corresponding matrices are modified accordingly. An attractive feature of this formulation is that the matrices involved are dimensionally small, making the numerical computation in the two stages of the process simple. Additionally, the Kalman filter only requires knowledge of the current sample and thus can be implemented in real time and across large networks.

Optimal Smoothing

Applying the Kalman filter in the forward direction solves what is known as the prediction problem, but if data are available over some interval and all that data past and future are used in the estimation, then the estimate at any given point can be improved. This is known as the smoothing problem and is a non-real-time or batch operation, but can also be implemented in near-real-time by limiting the smoothing to short intervals of time. The fixed interval smoother incorporates the maximal amount of information (compared with other smoothing algorithms) and consists of three conceptual steps: the forward Kalman filter described in the previous section, then a backward filter known as the information filter which is applied in reverse time order to the entire time series. The first two steps provide separate streams of information which are combined in the third step to compute the final state estimates.

Rauch *et al.* (1965) showed that the forward and information filters could be applied in a single step, which is referred to as the Rauch Tung Striebel (RTS) smoother. The smoother gain, which is analogous to the Kalman gain as it defines the amount of smoothing, is given by

$$\mathbf{F}_k = \mathbf{P}_k^f \mathbf{A}(\mathbf{P}_{k+1}^{f-})^{-1}, \qquad (25)$$

where $\mathbf{P}_{k+1}^{f-}$ and $\mathbf{P}_k^f$ are the *a priori* and *a posteriori* covariance matrices, respectively, from the forward filter. The smoothed covariances are given by

$$\mathbf{P}_k = \mathbf{P}_k^f - \mathbf{F}_k(\mathbf{P}_{k+1}^{f-} - \mathbf{P}_{k+1})\mathbf{F}_k^T, \qquad (26)$$

and the smoothed estimates by

$$\hat{\mathbf{x}}_k = \hat{\mathbf{x}}_k^f + \mathbf{F}_k(\hat{\mathbf{x}}_{k+1} - \hat{\mathbf{x}}_{k+1}^{f-}). \qquad (27)$$

Note that the smoothing stage works backward in time using the $k + 1$th timestep to estimate the kth step, and it does not depend on the measurements or system inputs. The RTS smoother consists of applying the forward filter first, from equations (21)–(24), and then smoothing using equations (25)–(27). The RTS algorithm requires the totality of the Kalman filtered time series to be available as well as all the *a priori* estimates, covariances, and *a posteriori* covariances,

making it a very data-intensive operation and, thus, limited to postprocessing scenarios.

For near-real-time computation one can apply the RTS algorithm to segments of data by lagging N samples behind the end of the real-time stream. In this fashion it is assumed that the N samples behind the real-time stream constitute a complete time series, and the RTS smoother (equations 25–27) is applied to them. Initialization is performed by setting $\mathbf{x}_N = \mathbf{x}_k^f$ and $\mathbf{P}_0 = \mathbf{P}_k^f$. Notice that the smoother gain $\mathbf{F}_k$ in equation (25) multiplies the residual $\hat{\mathbf{x}}_{k+1} - \hat{\mathbf{x}}_{k+1}^{f-}$ for the multirate scenario where GPS and accelerometer sampling rates differ. We show that the important parameter in near-real-time smoothing with this scheme is the number of GPS samples over which one can smooth rather than the actual time lag.

Proof of Concept

Outdoor Shake Table Tests

A series of earthquake simulations were conducted in 2006–2007 on a full-scale seven-story reinforced concrete wall building at the George E. Brown, Jr. Network for Earthquake Engineering Simulation (NEES) Large High-Performance Outdoor Shake Table (LHPOST) at the University of California, San Diego (Panagiotou, 2008; Moaveni *et al.*, 2010). The four simulations allowed us to test the Kalman filter algorithms in a controlled environment. The LHPOST includes a 12.2 m × 7.6 m steel table platform (platen), a reinforced concrete reaction mass, two servo-controlled dynamic actuators with large servo-valves, a platen sliding system with hydrostatic pressure balance bearings, and a real-time multivariable MTS 469DU digital controller with an output of 1024 Hz in displacement. The system is uniaxial and oriented east–west. It can achieve maximum peak-to-peak displacement of ±0.75 m, velocity of ±1.8 m/s, and acceleration of ±3 g, with a frequency bandwidth of 0–20 Hz.

The building with a total height of 19.2 m and total weight of 250 metric tons was constructed on the shake table platen and subjected to four low- to high-intensity ground motions, as recorded by accelerometers during the 1971 M_w 6.6 San Fernando and 1994 M_w 6.7 Northridge earthquakes (Fig. 2). The lowest intensity input motion in earthquake 1 (EQ1) consisted of the longitudinal component from the VNUY station recorded during the San Fernando earthquake. The two medium intensity input motions were the transverse components recorded at the VNUY station during the San Fernando earthquake (EQ2), and the longitudinal component from the WHOX station was recorded during the Northridge earthquake (EQ3). The large intensity input motion corresponded to the near-fault Sylmar Olive View Med 360º record during the Northridge earthquake (EQ4), which induced significant nonlinear response. This last class of earthquakes is expected to have a 10% probability of exceedance every 50 years. For calibration purposes, the
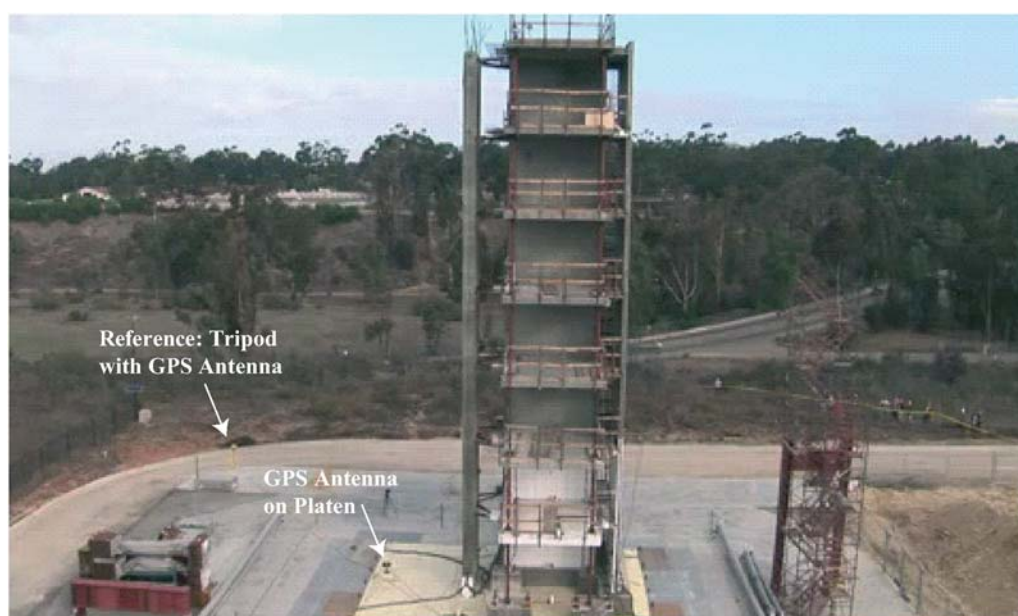
Figure 2.   George E. Brown, Jr. Network for Earthquake Engineering Simulation (NEES) Large High-Performance Outdoor Shake Table (LHPOST) at the University of California, San Diego with a to-scale seven-story reinforced concrete building. Seven 50 Hz GPS instruments were deployed just off the platen, two on the platen, four on the building foundation, three on the third floor, three on the fifth floor, and three on the roof of the building. A total of 15 MEMS accelerometers at a sampling rate of 240 Hz were deployed, two on the platen, four on the building foundation, three on the third floor, three on the fifth floor, and three on the roof of the building. The building was subjected to four strong-motion simulations (Table 1) from low to high intensity accelerometer records from the 1971 M_w 6.6 San Fernando and 1994 M_w 6.7 Northridge earthquakes. The color version of this figure is available only in the electronic edition.

earthquake records were preceded by a sinusoidal signal with peak-to-peak amplitude of about 0.15 m.

The building was instrumented with seven geodetic-quality Navcom NCT-200D GPS receivers sampling at 50 Hz and MEMS-Piezoresistive MSI model 3140 accelerometers sampling at 240 Hz. Three GPS receivers were mounted on the roof (seventh floor near the north, south, and east corners), and two receivers were cantilevered on the third and fifth floors of the flange wall (east side). A sixth receiver was located just off the shake table's platen as a stable reference point for measuring displacements. A seventh GPS receiver was situated on the platen. The 15 accelerometers were mounted as follows: 2 on the platen, 4 on the building foundation, 3 on the first floor, 3 on the fifth floor, and 3 on the seventh floor (roof). Unfortunately, the north receiver on the roof of the building was not operational during EQ4 due to a loose antenna cable.

GPS phase and pseudorange data were streamed to a PC workstation, and 50 Hz displacement waveforms were estimated on-the-fly using the method of instantaneous positioning described in the Real-Time Instantaneous Positioning section. The GPS-only displacements are relative to the fixed coordinates of the GPS receiver just off the platen, which were predetermined with respect to the true-of-date ITRF2005 coordinates of PBO station P472 at Camp Elliot (32º.8892 N, 117º.1047 W), approximately 656 m away. The accelerometer data were doubly integrated by high-pass filtering to determine accelerometer-only displacements.

We resampled the 240 Hz raw accelerometer data to 250 Hz to be able to align the times of every fifth point with the 50 Hz Navcom GPS data. Displacement waveforms were then computed using both the forward and the smoothed Kalman (RTS) filter using the GPS platen data as input and, in turn, the raw data from the two platen and four foundation accelerometers. To assess accuracy, we compared the GPS-only, accelerometer-only, and Kalman filter displacements with the input ground truth displacements provided at 1024 Hz by the MTS digital controller. To assess precision, we compared the root mean square (rms) of the distances between pairs of accelerometers and pairs of GPS receivers on the roof of the building (seventh floor). The results of these comparisons are given in Table 1.

Accuracy of the Displacement Waveforms

Accuracy was determined by comparing the various displacement waveforms with the truth displacements provided by the MTS recorder, for each of the four experiments, using the rms difference as the statistical measure. The results are given in Figure 3 and Table 1. The peak-to-peak displacements are on the order of 0.17 m for EQ1–EQ3, and 0.4 m for the high-intensity Northridge event (EQ4). The rms statistic is computed over the entire record including dynamic and static periods. The displacements for the single GPS on the platen have an rms difference of 2.6–4.0 mm, while the displacements for the two accelerometers on the platen have an rms difference of 12.0–19.3 mm. The larger differences

Table 1

RMS Differences between Computed Displacement Waveforms and the Input Registered by the Shake Table's MTS Recorder for Four Earthquake Simulations of Varying Intensity*

Sensor(s)	San Fernando Low Intensity	San Fernando Medium Intensity	Northridge Medium Intensity	Northridge High Intensity
GPS Displacements RMS (m)				
Platen GPS	0.0026	0.0040	0.0029	0.0037
Accelerometer-Derived Displacements RMS (m)				
PA1	0.0193	0.0181	0.0151	0.0120
PA2	0.0177	0.0184	0.0131	0.0175
FA1	0.0308	0.0278	0.0037	0.0027
FA2	0.0304	0.0274	0.0036	0.0028
FA3	0.0307	0.0276	0.0037	0.0027
FA4	0.0307	0.0276	0.0036	0.0027
Forward Filter RMS (m)				
PA1+GPS	0.0021	0.0041	0.0034	0.0033
PA2+GPS	0.0021	0.0041	0.0034	0.0033
FA1+GPS	0.0016	0.0021	0.0020	0.0020
FA2+GPS	0.0016	0.0020	0.0020	0.0020
FA3+GPS	0.0016	0.0021	0.0020	0.0020
FA4+GPS	0.0016	0.0021	0.0020	0.0020
Forward Filter+5 Hz Decimation RMS (m)				
PA1+GPS	0.0041	0.0074	0.0074	0.0046
PA2+GPS	0.0040	0.0074	0.0074	0.0046
FA1+GPS	0.0042	0.0067	0.0063	0.0037
FA2+GPS	0.0042	0.0066	0.0063	0.0037
FA3+GPS	0.0042	0.0066	0.0063	0.0037
FA4+GPS	0.0042	0.0066	0.0063	0.0037
Forward Filter+1 Hz Decimation RMS (m)				
PA1+GPS	0.0353	0.0211	0.0625	0.0341
PA2+GPS	0.0353	0.0211	0.0625	0.0341
FA1+GPS	0.0333	0.0313	0.0612	0.0273
FA2+GPS	0.0333	0.0305	0.0607	0.0265
FA3+GPS	0.0333	0.0308	0.0609	0.0275
FA4+GPS	0.0333	0.0309	0.0610	0.0277
Forward Filter + RTS Smoothing RMS (m)				
PA1+GPS	0.0016	0.0036	0.0024	0.0028
PA2+GPS	0.0016	0.0036	0.0024	0.0028
FA1+GPS	0.0017	0.0021	0.0021	0.0025
FA2+GPS	0.0017	0.0021	0.0021	0.0025
FA3+GPS	0.0017	0.0021	0.0021	0.0025
FA4+GPS	0.0017	0.0021	0.0021	0.0025
Forward Filter+RTS Smoothing+5 Hz Decimation RMS (m)				
PA1+GPS	0.0015	0.0038	0.0027	0.0028
PA2+GPS	0.0015	0.0038	0.0027	0.0028
FA1+GPS	0.0017	0.0022	0.0024	0.0025
FA2+GPS	0.0017	0.0022	0.0024	0.0025
FA3+GPS	0.0017	0.0022	0.0024	0.0025
FA4+GPS	0.0017	0.0022	0.0024	0.0025
Forward Filter+RTS Smoothing+1 Hz Decimation RMS (m)				
PA1+GPS	0.0077	0.0102	0.0152	0.0130
PA2+GPS	0.0077	0.0102	0.0152	0.0130
FA1+GPS	0.0097	0.0117	0.0168	0.0115
FA2+GPS	0.0097	0.0118	0.0166	0.0115
FA3+GPS	0.0098	0.0117	0.0167	0.0114
FA4+GPS	0.0096	0.0117	0.0167	0.0115
Roof Baselines RMS (m)				
GPS (N–S)	0.0033	0.0026	0.0035	-
GPS (N–E)	0.0030	0.0019	0.0034	-
GPS (S–E)	0.0036	0.0033	0.0023	0.0031
Accelerometer (N–S)	0.0008	0.0007	0.0010	0.0012

*Shown are the results of high-pass filtered accelerometer-derived displacements for platen accelerometers (PA1 and PA2) and building foundation accelerometers (FA1-4), as well as Kalman filtered waveforms obtained from the platen GPS and platen and foundation accelerometers. Shown are the results from decimated data (5 Hz for GPS and 100 Hz for accelerometers, and 1 Hz for GPS and 100 Hz for accelerometers). The peak displacements are 0.16–0.17 m for the first three simulations and 0.40 m for the fourth one.
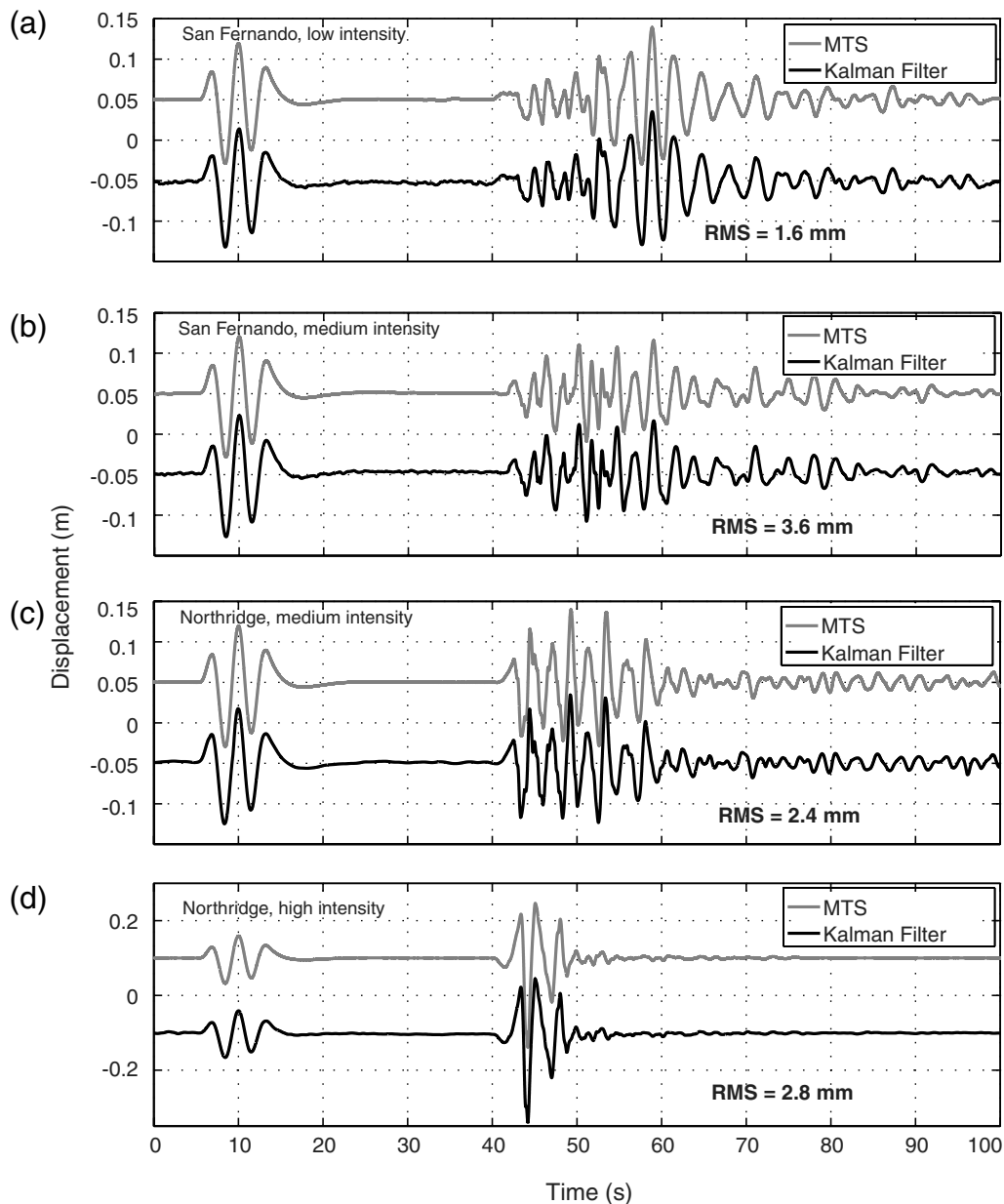
Figure 3. Accuracy of broadband displacement waveforms. Root mean square (rms) of the differences between the smoothed Kalman filter displacement waveforms estimated for the four earthquake simulations and the deterministic input as registered at 1024 Hz by the shake table's MTS digital recorder (see also Table 1). The waveforms are estimated from the platen GPS and one of the accelerometers on the platen. Note that the vertical scale is the same for (a) through (c) but changes for (d). The two waveforms in each graph have been offset for clarity.

for the accelerometer-derived displacements result from mismatches in amplitude and phase compared with the MTS displacements. The forward Kalman filter solutions reduce the rms differences by about 10% (except for EQ2, where there is a 10% increase) compared with the GPS-only solutions (2.2–4.1 mm), and there is an additional 10% improvement for all four experiments with the smoothed Kalman filter solutions (1.6–2.3 mm). For the foundation accelerometers, the rms differences are higher for EQ1 and EQ2 (about 30 mm), but unexpectedly an order of magnitude less for EQ3 and EQ4. In any case, we can conclude that the combined

GPS and accelerometer displacement waveforms provide overall millimeter-level accuracy over the entire range of sampled frequencies and improved accuracy when compared with GPS-only or accelerometer-only solutions. The improvement is generally more pronounced when compared with the accelerometer-only solutions. This is not surprising because of the inherent limitations and biases encountered in the double integration of accelerometer data. It is interesting to note that the rms statistics for either the static or dynamic periods did not differ significantly from the rms values computed for the entire period (static and dynamic) for

any of the experiments. We saw only insignificant degradation (∼10%) in accuracy during periods of strong shaking.

We repeated the previous analysis with two decimation schemes: the first one decimating the accelerometer to 100 Hz and the GPS to 5 Hz and the second one decimating the accelerometer to 100 Hz and the GPS to 1 Hz (Table 1). The latter corresponds to the sampling rates of real-time GPS and strong-motion sensors in southern California during the 2010 M_w 7.2 El Mayor–Cucapah earthquake. We find that the fit of the Kalman filtered waveforms is only mildly degraded in the first decimation scheme and significantly degraded with the second decimation scheme. However, smoothing provides a significant improvement, especially at the lower GPS sampling rates (1 Hz). This is an important practical consideration because GPS data are considerably more verbose than strong-motion data.

Precision of the Displacement Waveforms

In order to evaluate precision we examined the rms of the difference in displacements estimated for pairs of GPS and pairs of accelerometers on the roof of the building (seventh floor) for each of the four experiments (Table 1), including periods of both quiet and dynamic motion. The assumption is that the roof is rigid and that there is no permanent deformation occurring between the sensors. The displacements obtained from high-pass filtering of the accelerometer data show smaller rms differences on the order of only 1 mm, while the GPS-only displacements show rms differences on the order of 3 mm. This makes sense because accelerometer data are more sensitive to ground motion than GPS data, that is, they are more precise. However, as we have seen, accuracy is degraded for the accelerometer displacements due to biases in the double integration process, which in this case appear to be common to both accelerometers on the roof. GPS precision of about 3 mm is what we would expect from earlier studies of high-rate GPS horizontal displacements on short baselines (Genrich and Bock, 2006).

Application to the 2010 El Mayor–Cucapah Earthquake

The shake table experiments differed from a real-world event in several important ways. First, only the dynamic motions could be simulated. In a real event there would be no nearby stable GPS reference station, and displacements would need to be referred to one or more stations outside the region of deformation. Also, GPS noise would increase with longer station separations, by a factor of about 3 in the horizontal components and up to an order of magnitude in the vertical component (Langbein and Bock, 2004; Genrich and Bock, 2006). Finally, the ability to resolve integer-cycle phase ambiguities in real-time scenarios is diminished as station separations increase (e.g., Bock *et al.*, 2000). The 2010 M_w 7.2 El Mayor–Cucapah earthquake in northern Baja California and observations from southern California

high-rate GPS and very high-rate accelerometers provide us with a real-world event to highlight the advantages of combining GPS displacements and acceleration data.

The El Mayor–Cucapah earthquake broke a subset of northwest-trending strike-slip faults that are separated by pull-apart basins that accommodate northwest-southeast oriented extension and are parallel to the main strands of the San Andreas fault system (Imperial, Elsinore, San Jacinto, Laguna Salada, and Cerro Prieto faults). It caused significant ground motions at distances up to several hundred kilometers from the epicenter (Fialko *et al.*, 2010; Hauksson *et al.*, 2010). A robust set of 1 Hz GPS phase and pseudorange data were collected for this earthquake at 105 CRTN and PBO stations (Fig. 4), and on-the-fly displacement waveforms were estimated as described in the Real-Time Instantaneous Positioning section and posted on the GPS Explorer data portal (Webb *et al.*, 2009; see Data and Resources).

For this paper, we reprocessed the entire set of 1 Hz GPS-derived displacement waveforms (Fig. 5; see Data and Resources) in simulated real-time mode. We divided the network into nine subnetworks with at least two-station overlap and estimated relative displacement waveforms in the ITRF2005 frame for each subnetwork relative to an arbitrary station within each. The maximum relative motion encountered between adjacent stations closest to the epicenter was 0.58 m between stations P494 and P497 located 16.7 km apart (Fig. 4). Then we performed a network adjustment to estimate coordinates for all stations with respect to the true-of-date coordinates of station GNPS, and transformed the coordinates for each station into displacements in the local (N,E,U) frame using equation (1). GNPS was chosen, not because it is the farthest from the epicenter (it is 245 km to the northeast; Fig. 4), but because of directivity considerations.

We then combined the GPS-derived 1 Hz displacements with raw 100 Hz accelerometer data using the Kalman forward and smoothed filters to estimate the velocity and displacement waveforms. This was performed on a station-by-station basis for those 12 GPS stations that were within 1.5 km of an accelerometer. The instruments closest to the earthquake's epicenter were the accelerometer at WES and GPS at P494 (Table 2). The two sensors are about 72 km from the epicenter just north of the U.S.–Mexico border and 80 m from each other (Fig. 4). In Figure 6a, we show the entire period of seismic shaking at P494/WES in the vertical component. The observed broadband velocities clip even before the arrival of the *S* wave at the station, while the estimated velocity waveforms record the entire event at the 100 Hz rate of the accelerometer. In Figure 6b, we show the first 12 s of the vertical broadband velocity record at WES after the Southern California Earthquake Center's *P*-wave pick and overlay the Kalman-filter-estimated velocities (recall from Fusing GPS and Strong-Motion Accelerometer Data that the system states are displacement and velocity). That the broadband seismic data and the waveform estimated by Kalman smoothing are indistinguishable is striking, given also that the GPS resolution is poorest in the vertical direction. In Figure 6c, we compare
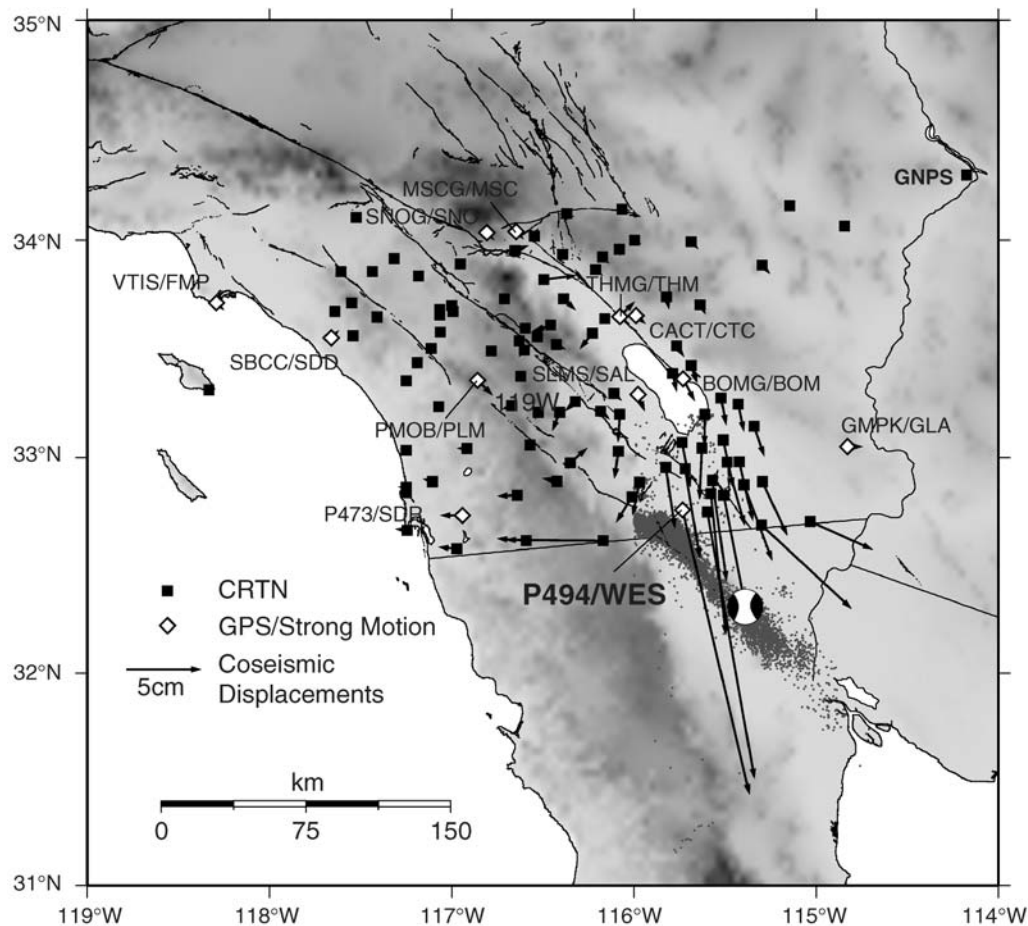
Figure 4.   California Real-Time GPS Network (CRTN) stations in southern California and collocated California Integrated Seismic Network (CISN) strong-motion accelerometer stations. The arrows indicate horizontal coseismic offsets from the 2010 M_w 7.2 El Mayor–Cucapah earthquake in northern Baja California (denoted by the focal mechanism). The 12 collocated stations (where the GPS and strong-motion accelerometers are within 1.5 km) are denoted by white diamonds. The GPS station name is given by its four-character code; the seismic station by its three-character code. P494/WES has a broadband seismometer, an accelerometer, and a GPS receiver and is featured in several subsequent figures.

displacements derived by (single) integration of the (12 s) seismometer record at WES, and the 100 Hz smoothed Kalman filter broadband displacements. It is clear that we can detect the small-amplitude *P*-wave recordings with a precision (and accuracy) of about 1 mm. This is a significant improvement over the 1 Hz GPS-only solutions where the vertical precision is on the order of several tens of millimeters, precluding *P*-wave detection. In a more realistic early warning scenario, we may not have 12 s of seismometer recordings, and we would have to rely completely on accelerometer data if no high-rate GPS were recorded.

Figure 6c also shows the poor results obtained by on-the-fly double integration of the accelerometer data. Of course, better results could be obtained after the fact (in post processing). To investigate this we computed displacements for WES from uncorrected double integration of accelerometer data (0th order correction), correcting with a function fitting procedure from Boore *et al.* (2002) (first-order correction, both linear and second order polynomial function fitting),

and with high-pass filtering (second-order correction). Although the dynamic motions could be extracted through baseline corrections or form fitting, the static displacements were lost. With the addition of high-rate GPS displacements, high-pass filtering or function fitting is not required, and the double integration can be performed on-the-fly using just the raw accelerometer records.

In Figure 7 we show the broadband displacement waveforms for P494/WES in all three components, where the 0.2 m horizontal static offset in the north component is clearly seen. The corresponding smoothed Kalman filter vertical displacement waveforms for P494/WES, as well as those for two other collocated GPS/accelerometer stations (BOMG/BOM and THMG/TGM, 129 km and 192 km from the epicenter, respectively; Fig. 4 and Table 2) are shown in Figure 8. In spite of the large epicentral distance and the diminished precision of the GPS vertical component, the Kalman filter with the aid of the accelerometer data is still capable of producing a precise waveform.
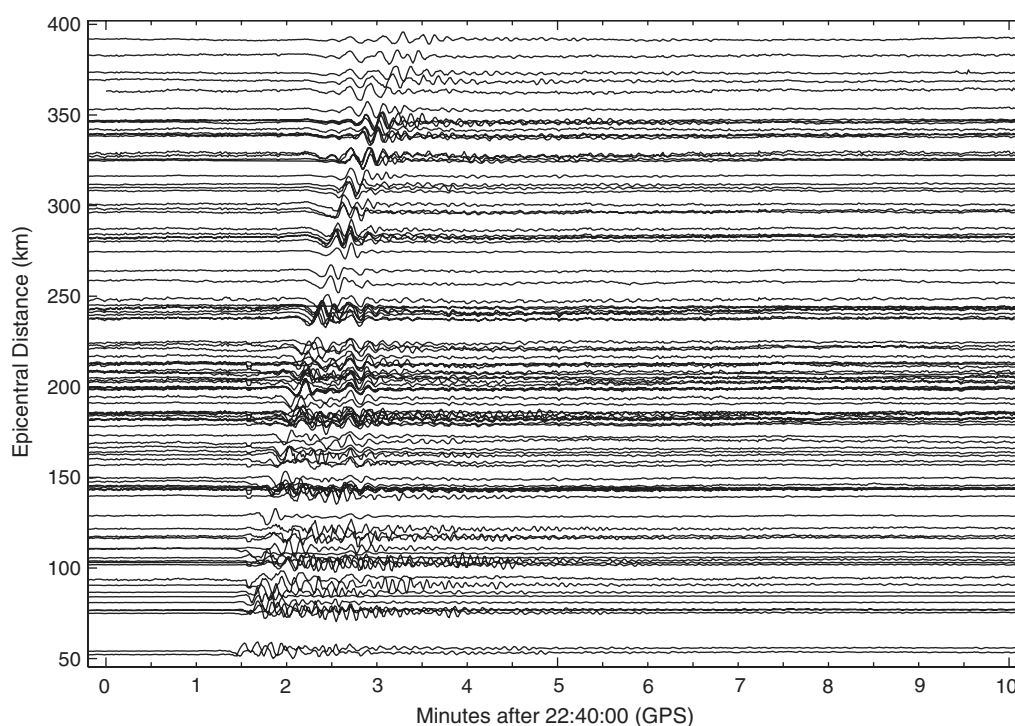
Figure 5. Displacements (1 Hz, east component) estimated for 105 CRTN stations are stacked according to epicentral distance for the 4 April 2010 M_w 7.2 El Mayor–Cucapah earthquake. The earthquake initiated at 22:40:40 UTC, or equivalently 22:40:55 GPS time. All waveforms have been normalized for clarity.

Spectral Characteristics of Displacement Waveforms

Spectral analysis of the smoothed Kalman filter displacement time series for the shake table experiments (Fig. 9a) and the El Mayor–Cucapah earthquake (Fig. 9b) highlights two attractive features: the power spectral densities follow the GPS-only spectrum at the low frequencies and the accelerometer-only spectrum at the high frequencies. This is desirable because it is in these two frequency bands that each instrument performs best (GPS at the lower frequencies and accelerometers at the higher frequencies). We can infer from the power spectral densities and the shake table experiments that the combined (100 Hz) waveform is more precise and accurate than the (1 Hz) GPS-only or (100 Hz) accelerometer-only displacement waveforms, and that we have achieved an accurate broadband record of this event.

The smoothed Kalman filter cannot be performed in real time because it requires both a forward and backward step. However, an examination of the spectral characteristics of the forward filter displacements indicates spurious spectral peaks that coincide with multiples of the GPS sampling frequency for both the shake table experiments (Fig. 10a) and the El Mayor–Cucapah earthquake (Fig. 10b). It is easy to see why this happens by examination of a blowup of 1 s of the unsmoothed forward time series for the shake table experiment (Fig. 11). In between the 50 Hz GPS samples, the series drifts during successive time updates when only new accelerometer data are available (every 250th of a second for the shake table and every 100th of a second for the earthquake).

But as soon as the next GPS measurement becomes available, there is an adjustment to the displacement time series explaining the observed sawtooth pattern, a pattern also evident in the El Mayor–Cucapah earthquake data. In Figure 12, we show the results of a synthetic test of a sawtooth with a period of 1 s and estimate its power spectral density using the multitaper method. It shows broad peaks centered at multiples of the sawtooth period, which corresponds to the GPS sampling frequency in our data sets. This is a minor problem because for real-time seismological applications the increase in noise introduced by the peaks is small compared with the signal. Furthermore, the increase in noise is only at frequencies higher than ~1–2 Hz. In any case, the fixed interval smoother removes the spurious peaks altogether, while the near-real-time smoother reduces the noise peaks as a function of the lag amount.

Selecting the Kalman Filter Variances

The Kalman filter has two parameters that dictate its performance, the measurement variance r and the system dynamics variance q. To maintain objectivity and to simulate a real-time environment, we compute the measurement variance from 50 s windows of preevent noise on the three components of the GPS displacements (Fig. 13). These tend to be very stable across a network, with the east component showing the least variance, then the north component, and the vertical component being the noisiest as expected, due to the satellite constellation configuration and unmodeled
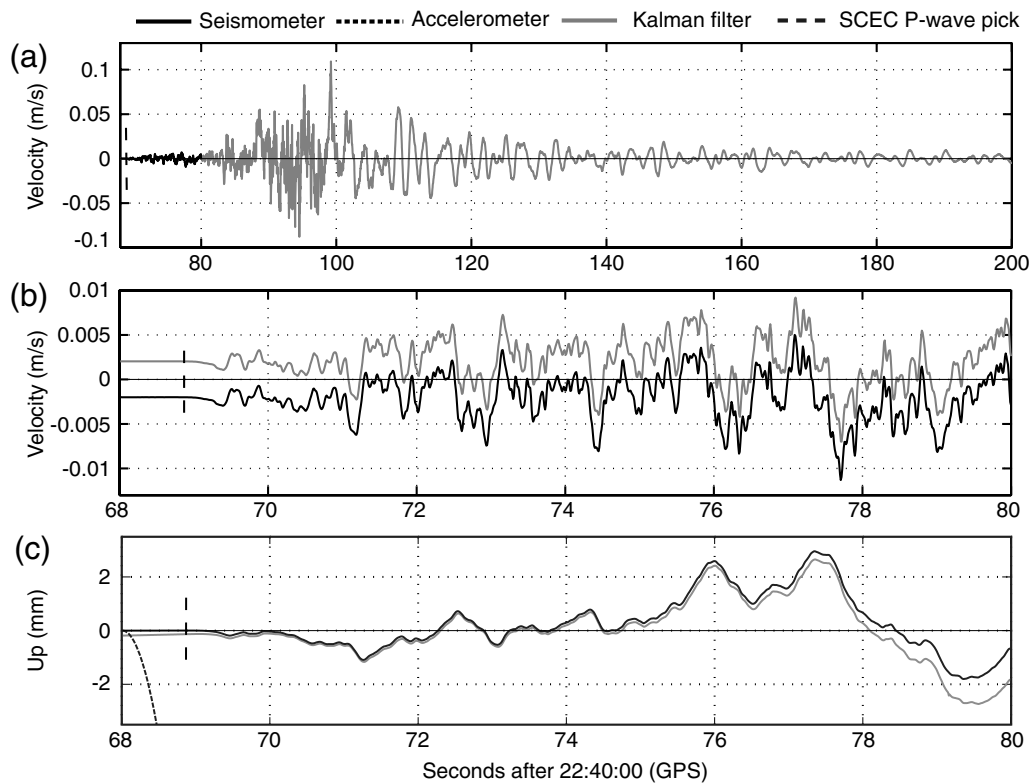
Figure 6. Estimation of unclipped velocity and displacement waveforms. (a) Comparison between vertical velocity records registered by a broadband seismometer at station WES (Fig. 4), which clipped 11 s after the onset of shaking and the smoothed Kalman filter estimated velocities for P494/WES. The El Mayor–Cucapah earthquake initiated at 22:40:55 GPS time on 4 April 2010. (b) Blowup of the same time series for its first 12 s showing essentially one-to-one agreement between the observed velocity and the estimated velocity waveforms. The two waveforms have been offset for clarity. The SCEC P-wave pick denoted by vertical dashes is at ~22:41:09 GPS time, or 29 s after earthquake initiation. (c) Comparison of single integration of the vertical seismometer record at WES, 100 Hz smoothed Kalman filter displacements (GPS/accelerometer), and double integration of only the accelerometer data. Note the magnitude of displacement, indicating that the broadband displacements have a precision and accuracy of about 1 mm.
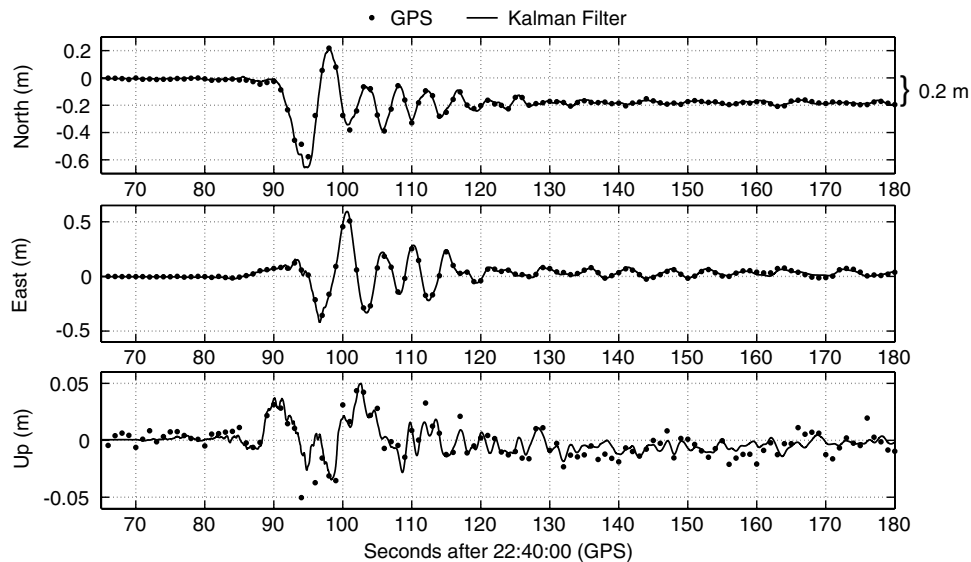
Figure 7. Comparison of 1 Hz GPS and 100 Hz smoothed Kalman filter displacement waveforms. Shown are 1 Hz GPS displacements for P494 and 100 Hz smoothed Kalman filter displacements for P494/WES. The El Mayor–Cucapah earthquake initiated 22:40:55 GPS time on 4 April 2010. The SCEC P-wave pick for station WES is at ~22:41:09 GPS time. Note the 0.2 m static (coseismic) offset in the north component.

Table 2
Collocated GPS (California Real-Time GPS Network) and Strong-Motion Accelerometer (California Integrated Seismic Network) Stations with a Station Separation of 1.5 km or Less

CRTN Station	Latitude (°N)	Longitude (°W)	CISN Station	Latitude (°N)	Longitude (°W)	Separation (km)
P473	32.7338	116.9495	SDR	32.7356	116.9424	0.70
P494	32.7597	115.7321	WES	32.7590	115.7316	0.08
GMPK	33.0511	114.8273	GLA	33.0512	114.8271	0.05
SLMS	33.2922	115.9778	SAL	33.2801	115.9859	1.50
PMOB	33.3572	116.8595	PLM	33.3536	116.8626	0.50
BOMG	33.3646	115.7297	BOM	33.3647	115.7296	0.01
SBCC	33.5530	117.6615	SDD	33.5526	117.6617	0.05
THMG	33.6506	116.0773	THM	33.6507	116.0773	0.01
CACT	33.6551	115.9900	CTC	33.6551	115.9901	0.01
VTIS	33.7126	118.2938	FMP	33.7126	118.2938	0.00
SNOG	34.0352	116.8078	SNO	34.0352	116.80778	0.01
MSCG	34.0385	116.6480	MSC	34.0385	116.6480	0.00

tropospheric refraction (Bock *et al.*, 2000). The observed GPS variances are consistent with the results of Genrich and Bock (2006).

Estimating the system dynamics variance is more complicated. At first glance it could be determined simply by taking the variance of windows of preevent accelerometer noise. However, there are several sources of noise in the accelerometer that preclude this. Perhaps the most important is sensor rotation and tilt (Trifunac and Todorovska, 2001) whose net effect is to raise the noise floor. This does not manifest itself until shaking starts and is thus not present in preevent noise estimation. Trifunac and Todorovska (2001) show that as one utilizes an increasing number of bits to digitize the transducer signal and as earthquake magnitude increases, the problem becomes more insidious. Lee and Trifunac (2009)

obtain empirical relations for computing the Fourier spectra of rotation and tilt from translational acceleration spectra. The empirical relations depend on multiple factors including magnitude, focal depth, soil conditions, thickness of the sedimentary layer, and epicentral distance. When compared with the amplitudes of processing and recording noise they find that the most extreme behavior of the rotational and tilting spectra is about three orders of magnitude greater than translational noise levels. We show the effect of using q measured from preevent noise windows by taking the more extreme value of $1000 \times q$ as the system dynamics variance for input into the Kalman filter. In Figure 14a we show the east component (because it displays the largest sensitivity to changes in q) and observe that when applying the forward Kalman filter without smoothing and comparing it with GPS measurements,
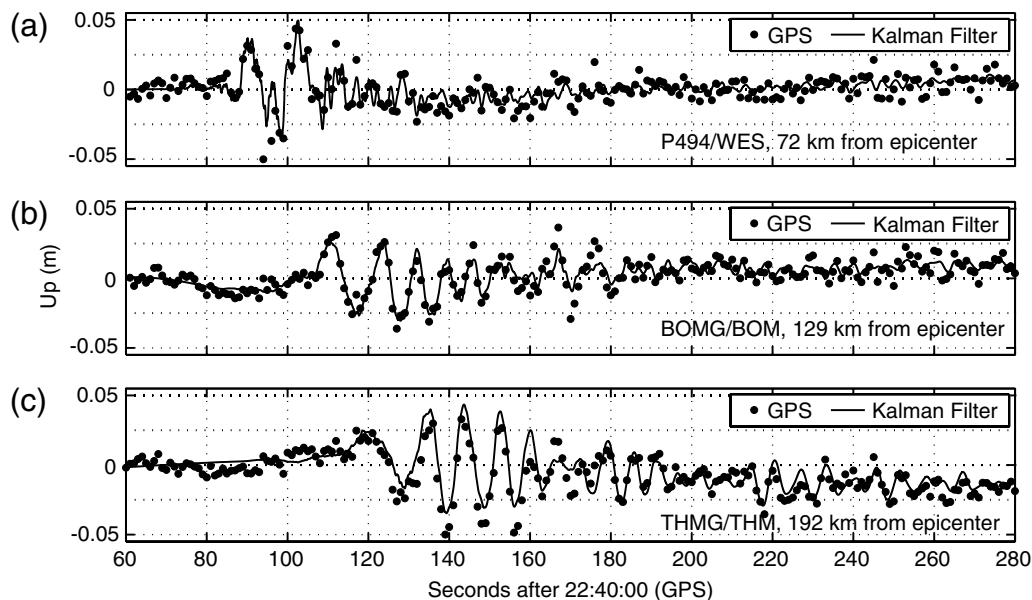

Figure 8. Vertical displacement waveforms. Comparison of 1 Hz GPS and 100 Hz smoothed Kalman filter estimates for (a) P494 and P494/WES, (b) BOMG and BOMG/BOM, (c) THMG and THMG/THM. The El Mayor–Cucapah earthquake initiated at 22:40:55 GPS time on 4 April 2010.
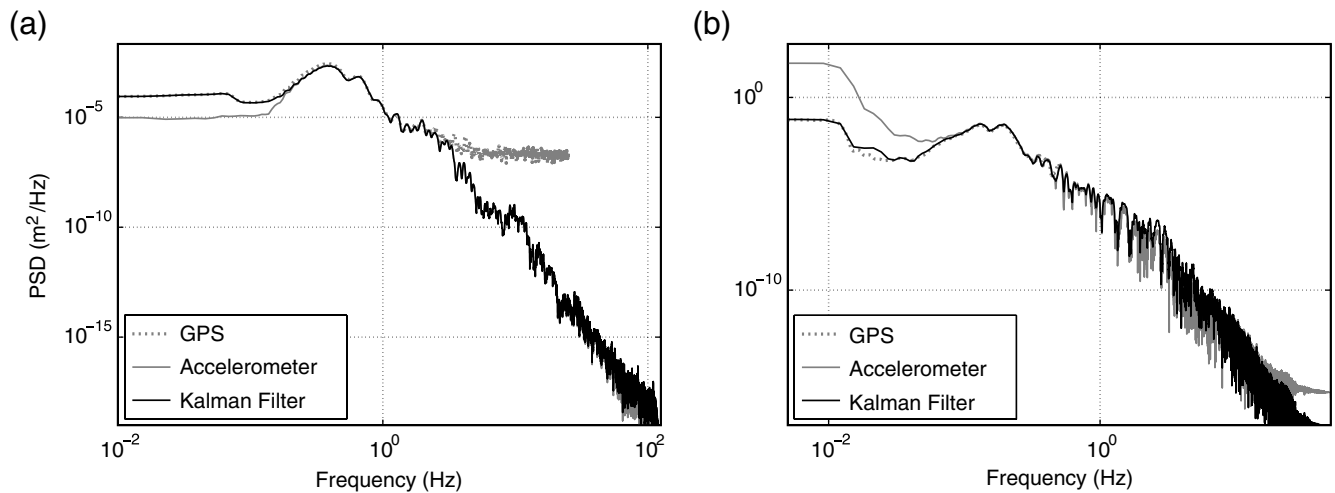
Figure 9. Power spectral densities. (a) High intensity Northridge earthquake simulation (EQ4) on shake table platen for 50 Hz GPS-only displacements, 240 Hz accelerometer-derived high-pass filtered displacements, and 250 Hz smoothed Kalman filter displacements; (b) 2010 El Mayor–Cucapah earthquake for 1 Hz GPS displacements at P494, 100 Hz accelerometer-derived high-pass filtered displacements at WES, and 100 Hz smoothed Kalman filter displacements for P494/WES.
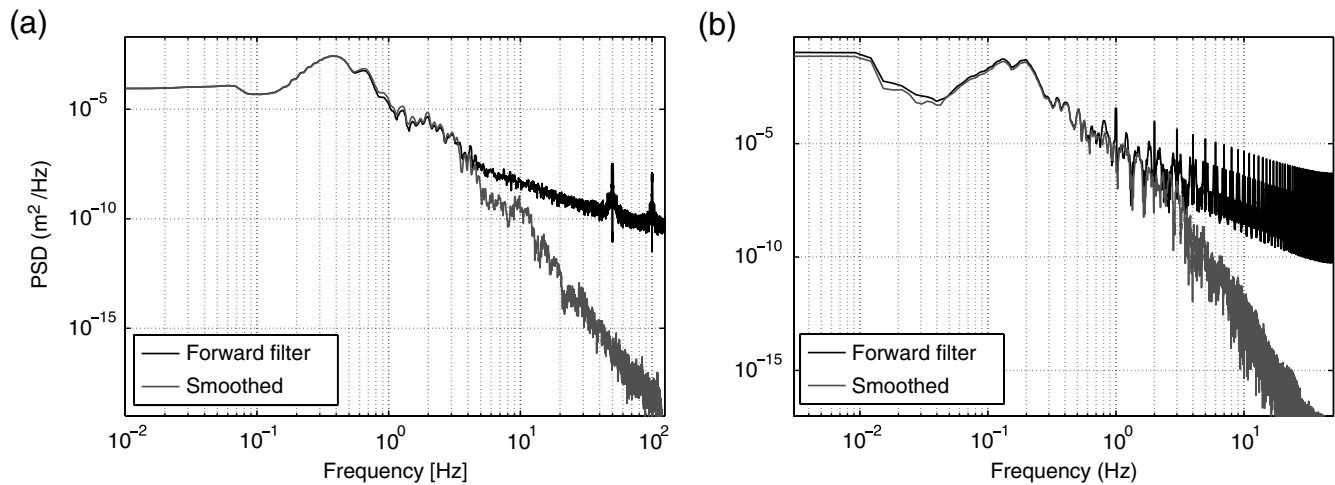

Figure 10. Power spectral density comparisons between forward Kalman filter and smoothed Kalman filter displacements waveforms for (a) high-intensity Northridge earthquake simulation (EQ4) 250 Hz displacements on shake table platen; (b) 2010 El Mayor–Cucapah earthquake 100 Hz displacements for P494/WES. Note the spikes in the forward filter corresponding to the GPS sampling frequency, 50 Hz for (a) and 1 Hz for (b).
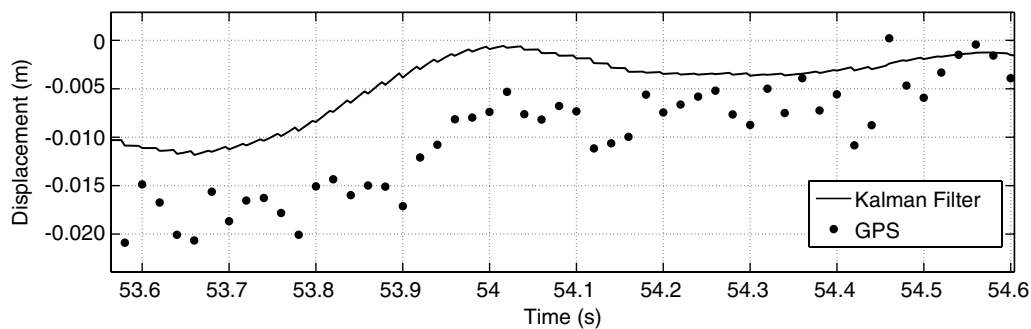
Figure 11. Example of sawtooth-like irregularities introduced by the disparity in sensor sampling frequencies. Shown is a blowup of the high intensity Northridge earthquake simulation (EQ4) with a 250 Hz sampling frequency for the forward Kalman filter displacements and 50 Hz sampling frequency for the GPS-only displacements.
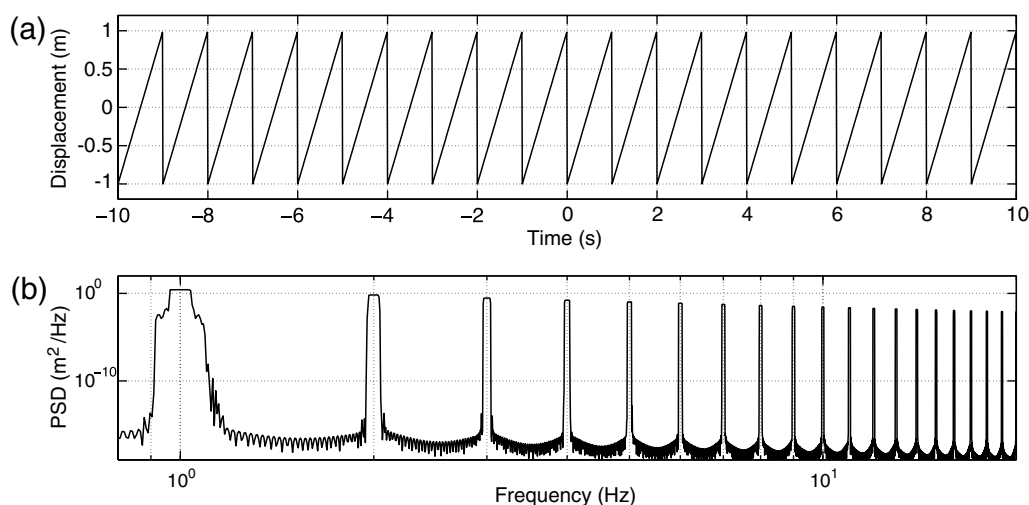
Figure 12. (a) 1 Hz sawtooth function and (b) its power spectral density.

the filter miscomputes the resulting static displacements by as much as 0.08 m. If we adjust the variance to $1000 \times q$, then the static offset is adequately recovered but the amplitudes of dynamic shaking can vary by as much as 0.25 m.

In spite of these large variations, the problem becomes, in effect, moot using Kalman smoothing, where using q or $1000 \times q$ has a very limited effect on the recovered waveform (Fig. 14b). Applying a near-real-time smoother with a 10 s lag, even with an extreme value of the variance, fully recovers the waveform (Fig. 14c). We find that the 10 s lag, in this case, is the minimum necessary to recover an adequate waveform, that is, one without bias in dynamic shaking amplitude or in static offset. This lag, however, might be too long for real-time applications in which case the sampling rate of the GPS must be increased to reduce the lag of the near-real-time smoother (recall that misfits arise from the sawtooth pattern effect of GPS sampling frequency). Alternatively, if the station conditions are known, the empirical relations of Lee and Trifunac (2009) can be used to assess the proper scaling of q.
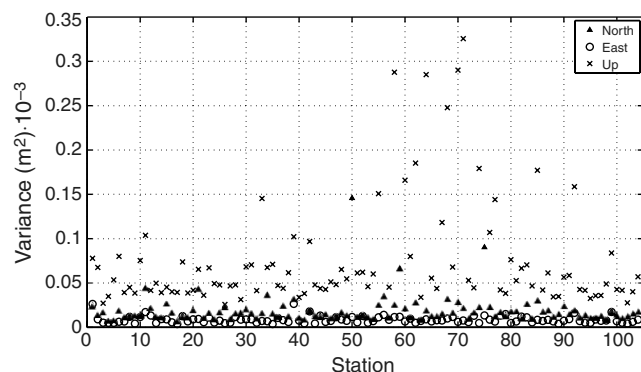
Figure 13. Variances for 50 s of displacements for some California Real-Time GPS Network (CRTN) stations estimated prior to the 2010 El Mayor–Cucapah earthquake in the north, east, and vertical (up) components.

Discussion

We have described the estimation of strong-motion broadband displacement waveforms using an optimal combination of collocated high-rate GPS and very high-rate accelerometer data. In this section, we elaborate on a number of issues and provide some directions for future work.

The very high-frequency response of GPS-derived displacements is flat above 0.05–0.5 Hz (< 2–20 s) so that GPS data are capable of providing essentially uncorrelated single-epoch estimates of displacement over a large range of seismic frequencies at the (10–50 Hz) sampling rate of modern GPS receivers (Genrich and Bock, 2006). The CRTN project has demonstrated that 10 Hz data can be reliably streamed over dedicated microwave and radio modem communication links provided by the University of California, San Diego's High-Performance Wireless Research and Education Network project (HPWREN; see Data and Resources), but this requires a tenfold increase in the transmitted data compared with the current 1 Hz rate. The PBO project streams 1 Hz data from their GPS stations but stores 10 Hz measurements in receiver memory that can be downloaded in the case of a significant seismic event. It is not practical to stream at higher data rates with current limitations in cellular communications. A more cost-effective approach is to, wherever possible, add accelerometer instruments at existing GPS stations, stream the very high-rate but lower volume accelerometer data over the same communications links as the GPS data, and use the Kalman filter to optimally combine both data sets. This approach provides displacements at the sampling rate of the accelerometers (e.g., 100 Hz) with the precision of the accelerometer data and the accuracy of the GPS data. Our shake table results indicate that there is little benefit in increasing the GPS sampling rate to greater than 5 Hz.

We find that a very basic state vector representation is sufficient for the Kalman filter, where the acceleration
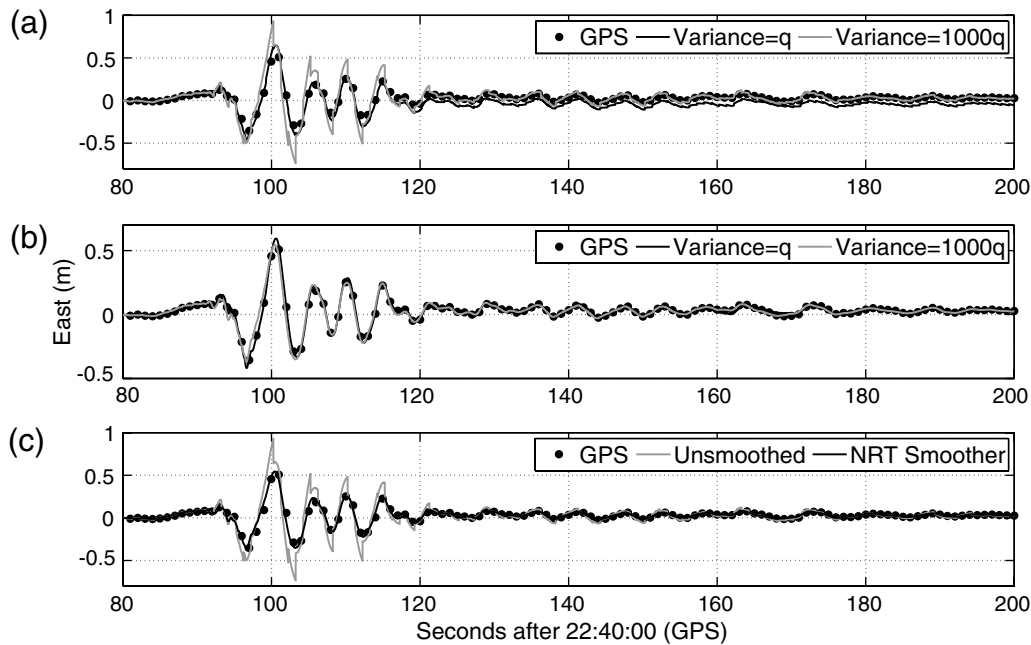
Figure 14. Effect of choice of system dynamics variance in Kalman filter estimation in the east component. (a) Comparison between forward Kalman filter waveforms using q and $1000q$ as the system dynamics variance, where q is the preevent variance estimate for the accelerometer data. The forward filter can be performed in real time. (b) Comparison between RTS smoothed waveforms using q and $1000q$ as system dynamics variance. The RTS smoother is limited to postprocessing because it requires a backward step through the entire data set. (c) Comparison between forward Kalman filter and smoothed Kalman filter with a lag of 10 s using $1000q$. The smoothed filter can be performed in near real time.

driving the system is assumed to be constant in between timesteps. There is no apparent need for additional state vector parameters, for example, possible tilts or other biases in the accelerometer data. Furthermore, it is not critical to characterize the variance factor q for the raw accelerometer data, because the corresponding GPS variance factor r is well known, and the high-rate GPS displacements are uncorrelated from epoch to epoch. This has been demonstrated in previous work (e.g., Genrich and Bock, 2006) and further verified in this paper. In fact, one can provide an overly pessimistic value for the accelerometer variance factor (say $1000 \times q$, or 1000 times the preevent noise) because the periodic GPS displacement measurements are sufficiently accurate to provide tight constraints on the single and double integration of accelerometer data to velocity and displacement, which is implicit in the Kalman filter formulation. One way to explain this is that the GPS displacements allow one to use definite integrals in the integration process by providing for explicit constants of integration, that is, we can take full advantage of the first fundamental theorem of calculus. Without the GPS displacements, the integration process is somewhat indefinite due to noise, accelerometer biases, and the limited dynamic range in seismometers. In addition, the effect of overestimating the system dynamics variances is nullified if a smoother is employed. Similarly, introduction of the accelerometer data stream into the Kalman filter helps to better estimate vertical static and dynamic displacements, which are noisy in a GPS-only scenario. This improved estimation of vertical

motion could have important applications in the analysis of tsunamigenic earthquakes.

We compare the north components of the estimated displacement waveforms from GPS alone (Fig. 15a) with those estimated using the smoothed Kalman filter (Fig. 15b) for 12 collocated stations (Table 2). The signal quality improves significantly in the latter. The preevent noise levels are lower, and the artifacts in the GPS waveforms (at 1.6 min and 5 min in Fig. 5 and at 95 s in Fig. 15a) are eliminated. The artifacts are due primarily to variations in position of the GPS reference station(s). These variations will propagate to all other stations in the network and are due to random and systematic errors in the GPS data and/or analysis and could be mistaken for actual seismic phases. These improvements have important implications for the use of GPS displacements as part of the earthquake early warning systems, which currently use only seismic data (Gasparini et al., 2007). GPS displacements provide better constraints than seismic data alone, in particular for large earthquakes, help confirm that a large earthquake has occurred, and reduce the amount of time required to issue a reliable alert regarding the earthquake's magnitude. The optimal combination of GPS displacements with accelerometer data provides distinct advantages as was dramatically demonstrated for the El Mayor–Cucapah earthquake, where the P-wave arrivals could be detected in the combined solution, taking advantage of the greater precision of the accelerometers. They were not detectable in the GPS-only approach because of the reduced sensitivity of GPS to vertical
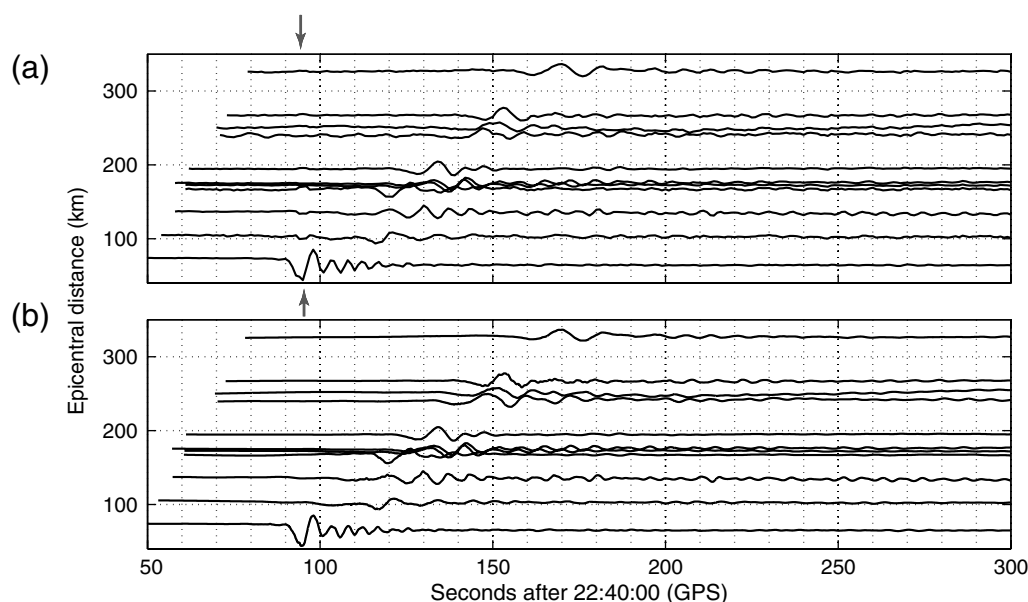
Figure 15. Broadband displacement waveforms in the east component for (a) 1 Hz GPS only and (b) smoothed Kalman filter solutions for 12 collocated GPS/seismic stations in southern California (Fig. 4). Note the artifact (denoted by gray arrows) introduced by the GPS network adjustment at 95 s in (a), which is absent in (b), and the flatter (more precise) preevent displacements in (b) compared with (a). The El Mayor–Cucapah earthquake initiated at 22:40:40 UTC (22:40:55 GPS time) on 4 April 2010. All waveforms have been normalized for clarity.

motions. The detection of the *P*-wave arrival is critical for earthquake early warning, as it allows for prediction of the arrival of the destructive *S* wave.

We noted that there are certain limitations in the real-time estimation of displacements from GPS phase and pseudorange data. The introduction of very high-rate precise accelerometer data at the GPS stations could help reduce the problems discussed previously in real-time applications by introducing independent confirmation of significant station displacement. For this purpose, we are considering a more tightly coupled Kalman filter (Jekeli, 2001). Instead of analyzing the already estimated GPS displacements with the raw accelerometer data, one could design a Kalman filter that instead uses the raw GPS phase and pseudorange observations and the raw accelerometer data, in order to improve the on-the-fly resolution of phase ambiguities. It should be noted that the availability of modernized GPS signals (L2C and L5) and other Global Navigation Satellite System (GNSS) satellite signals should also improve the overall robustness of the integrated GPS/seismic approach, as well as the GPS-only approach.

Other important issues include siting, monumentation, and mounting of GPS and seismic instruments at collocated stations. One question not addressed in this paper is whether costs can be reduced by using less sensitive and cheaper accelerometers, or whether the current practice of installing high-end accelerometers in boreholes is necessary.

Conclusions

The M_w 7.2 El Mayor–Cucapah earthquake on 4 April 2010 in northern Baja California demonstrated convincingly

that regional high-rate real-time GPS networks can become an essential tool for early warning and rapid earthquake response. We took this one step further by applying a Kalman filter to obtain an optimal combination of data from collocated high-rate GPS and very high-rate accelerometer stations, which takes advantage of the strengths and minimizes the weaknesses of both data types. The result is a new methodology for providing displacement time series with millimeter precision that can be used to better characterize the seismic source. It provides an improved broadband record of ground displacements and velocities over the full range of frequencies sampled by the accelerometer data, as well as the static deformation. Our approach is capable of precisely detecting *P*-wave arrivals of medium to large near-source earthquakes with dense networks of collocated GPS and seismic instruments, making it particularly valuable for earthquake early warning systems and rapid earthquake response. It also provides a powerful new analysis tool to study the rupture characteristics of large earthquakes.

Data and Resources

All the websites listed in this section were current as of September 2011. Web sources mentioned in the paper include NEES @ UC San Diego Large High-Performance Outdoor Shake Table (http://nees.ucsd.edu/); JPL's NASA Global Differential GPS (GDGPS) System (www.gdgps.net/); ITRF2008 reference frame (http://itrf.ensg.ign.fr/ITRF_solutions/2008/); International GNSS Service (http://igscb.jpl.nasa.gov/). GPS data at a 1 Hz rate collected by the California Real Time (GPS) Network (CRTN) are archived in 24-hour

segments at the SOPAC GARNER GPS archive anonymous ftp://garner.ucsd.edu/pub/highrate/cache/rinex/. GPS RINEX data at a 5 Hz rate collected by the PBO are available in hourly segments at the SOPAC archive for the day of the El Mayor–Cucapah earthquake at anonymous ftp://garner.ucsd.edu/pub/highrate/cache/rinex/2010/094.5hz/, as well as for the two days prior and two days following 4 April 2010. SOPAC maintains a web page for the California Real Time (GPS) Network (CRTN) project (http://sopac.ucsd.edu/projects/realtime/). CRTN data at a 1 Hz rate can be streamed in real-time as described in http://sopac.ucsd.edu/input/realtime/CRTN_Access.xls in three formats: RTCM 2.3, RTCM 3.0, and GPS receiver-dependent raw data formats for certain stations. 1 Hz GPS-only displacement waveforms for the El Mayor–Cucapah earthquake from 105 CRTN and PBO stations are available from a special portlet on GPS Explorer (http://geoapp03.ucsd.edu/gridsphere/gridsphere?cid=Mayor-Cucapah+Earthquake). 100 Hz Kalman-smoothed displacements for the El Mayor–Cucapah earthquake for 12 collocated GPS/seismic stations (Table 2) are also available on GPS Explorer. Three component 1 Hz GPS seismograms for 105 stations and 100 Hz GPS/seismic seismograms for 12 collocated stations (Table 2) are available in SAC format at SCEDC (www.data.scec.org/research/MayorCucapah20100404/Mexicali_GPSsac.tar.gz). The following data are available on request from the University of California, San Diego Shake Table experiments: 50 Hz GPS displacement waveforms from 6 receivers; 240 Hz raw accelerometer data from 15 accelerometers; 1024 Hz MTS data; and 250-Hz Kalman-smoothed displacements. GPS displacements and raw accelerometer data were analyzed with a Kalman filter (forward and smoothing) software written by Melgar and Bock in Matlab. The software modules are available upon request.

Acknowledgments

References

Allen, R. M., P. Gasparini, and O. Kamigaichi (Editors), (2009). New methods and applications of earthquake early warning, *Geophys. Res. Lett.* **36,** special section, L00B05, L00B08, L00B03, L00B04, L00B02, L00B06, L00B01, L00B07.

Astiz, L. (Editor) (2009). Special issue on earthquake early warning, *Seismol. Res. Lett.* **80,** no. 5.

Bar-Sever, Y., G. Blewitt, R. S. Gross, W. C. Hammond, V. Hsu, K. W. Hudnut, R. Khachikyan, C. W. Kreemer, R. Meyer, H.-P. Plag, M. Simons, J. Sundstrom, Y. Song, and F. Webb (2009). A GPS Real Time Earthquake And Tsunami (GREAT) alert system, *Eos Trans. AGU* **90,** no. 52, Fall Meet. Suppl., Abstract G21A-02.

Bassis, J. N., H. A. Fricker, R. Coleman, Y. Bock, J. Behrens, D. Darnell, M. Okal, and J.-B. Minster (2007). Seismicity and deformation associated with ice-shelf rift propagation, *J. Glaciol.* **53,** 523–536.

Blewitt, G. (1989). Carrier phase ambiguity resolution for the Global Positioning System applied to geodetic baselines up to 2000 km, *J. Geophys. Res.* **94,** 10187–10203.

Blewitt, G., W. C. Hammond, C. Kreemer, H.-P. Plag, S. Stein, and E. Okal (2009). GPS for real-time earthquake source determination and tsunami warning systems. *J. Geodes.* **83,** 335–343, doi 10.1007/s00190-008-0262-5.

Blewitt, G., C. Kreemer, W. C. Hammond, H. P. Plag, S. Stein, and E. Okal (2006). Rapid determination of earthquake magnitude using GPS for tsunami warning systems, *Geophys. Res. Lett.* **33,** doi 10.1029/2006GL026145.

Bock, Y., R. Nikolaidis, P. J. de Jonge, and M. Bevis (2000). Instantaneous geodetic positioning at medium distances with the Global Positioning System, *J. Geophys. Res.* **105,** 28,233–28,253.

Bock, Y., L. Prawirodirdjo, and T. I. Melbourne (2004). Detection of arbitrarily large dynamic ground motions with a dense high-rate GPS network, *Geophys. Res. Lett.* **31,** doi 10.1029/2003GL019150.

Boore, D. M. (2001). Effect of baseline corrections on displacements and response spectra for several recordings of the 1999 Chi-Chi, Taiwan, earthquake, *Bull. Seismol. Soc. Am.* **91,** 1199–1211.

Boore, D. M., C. D. Stephens, and W. B. Joyner (2002). Comments on baseline correction of digital strong-motion data: Examples from the 1999 Hector Mine, California, earthquake, *Bull. Seismol. Soc. Am.* **92,** 1543–1560.

Böse, M., and T. Heaton (2010). Probabilistic prediction of rupture length, slip and seismic ground motions for an ongoing rupture: Implications for early warning for large earthquakes, *Geophys. J. Int.* **183,** 1014–1030, doi 10.1111/j.1365-246X.2010.04774.x.

Cervelli, P. F., T. Fournier, J. Freymueller, and J. A. Power (2006). Ground deformation associated with the precursory unrest and early phases of the January 2006 eruption of Augustine Volcano, Alaska, *Geophys. Res. Lett.* **33,** doi 10.1029/2006GL027219.

Chui, C. K., and G. Chen (2009). *Kalman Filtering with Real-Time Applications*, Fourth Ed., Springer, New York, 229 pp.

Crowell, B., Y. Bock, and M. Squibb (2009). Demonstration of earthquake early warning using total displacement waveforms from real time GPS networks, *Seismol. Res. Lett.* **80,** 772–782, doi 10.1785/gssrl.80.5.772.

Dong, D. N., and Y. Bock (1989). Global Positioning System network analysis with phase ambiguity resolution applied to crustal deformation studies in California, *J. Geophys. Res.* **94,** 3949–3966.

Emore, G., J. Haase, K. Choi, K. M. Larson, and A. Yamagiwa (2007). Recovering seismic displacements through combined use of 1-Hz GPS and strong-motion accelerometers, *Bull. Seismol. Soc. Am.* **97,** 357–378, doi 10.1785/0120060153.

Fialko, Y., A. Gonzalez, J. J. Gonzalez-Garcia, S. Barbot, S. Leprince, D. T. Sandwell, and D. C. Agnew (2010). Static rupture model of the 2010 *M* 7.2 El Mayor–Cucapah earthquake from ALOS, ENVISAT, SPOT and GPS Data, Abstract T53B-2125 presented at *2010 Fall Meeting, AGU*, San Francisco, California, 13–17 December.

Gasparini, P., G. Manfredi, and J. Zschau (Editors) (2007). *Earthquake Early Warning Systems*, Springer, New York.

Geng, J. (2010). Rapid integer ambiguity resolution in GPS precise point positioning, *Ph.D. Thesis*, University of Nottingham, Nottingham, United Kingdom.

Genrich, J. F., and Y. Bock (2006). Instantaneous geodetic positioning with 10–50 Hz GPS measurements: Noise characteristics and

implications for monitoring networks, *J. Geophys. Res.* **111,** doi 10.1029/2005JB003617.

Graizer, V. M. (1979). Determination of the true ground displacement by using strong motion records, *Izvestiya Phys. Solid Earth* **15,** 875–885.

Gutman, S. I. (2008). *Troposphere signal delay corrections*, http://gpsmet .noaa.gov/downloads/Trop_Delay_Corrections.pdf (last accessed September 2011).

Hammond, W. C., B. A. Brooks, R. Bürgmann, T. Heaton, M. Jackson, and A. R. Lowry (2010). *The Scientific Value of High-Rate, Low-Latency GPS Data,* http://unavco.org/community_science/science_highlights/ 2010/RealTimeGPSWhitePaper2010.pdf (last accessed September 2011).

Hauksson, E., J. Stock, K. Hutton, W. Yang, J. A. Vidal-Vilelgas, and H. Kanamori (2010). The 2010 M_w 7.2 El Mayor–Cucapah earthquake sequence, Baja California, Mexico and southernmost California, USA: Active seismotectonics along the Mexican Pacific margin, *Pure Appl. Geophys.* **168,** doi 10.1007/s00024-010-0209-7.

Heaton, T. (1985). A model for a seismic computerized alert network, *Science* **228,** 987–990, doi 10.1126/science.228.4702.987.

Iwan, W. D., M. A. Mooser, and C. Y. Peng (1985). Some observations on strong motion earthquake measurements using a digital accelerograph, *Bull. Seismol. Soc. Am.* **75,** 1225–1246.

Jackson, M. (2003). Geophysics at the speed of light: EarthScope and the Plate Boundary Observatory, *The Leading Edge* **22,** 262–267, doi 10.1190/1.1564532.

Jekeli, C. (2001). *Inertial Navigation Systems with Geodetic Applications* Walter de Gruyter, Berlin, Germany, 252 pp.

Ji, C., K. M. Larson, Y. Tan, K. W. Hudnut, and K. Choi (2004). Slip history of the 2003 San Simeon earthquake constrained by combining 1-Hz GPS, strong motion, and teleseismic data, *Geophys. Res. Lett.* **31,** L17608, doi 10.1029/2004GL020448.

Kalman, R. E. (1960). A new approach to linear filtering and prediction problems, *Trans. ASME J. Basic Eng.* **82,** 35–45.

Kanamori, H., and L. Rivera (2008). Source inversion of W phase: speeding up seismic tsunami warning, *Geophys. J. Int.* **175,** 222–238.

Kedar, S., S. Watada, and T. Tanimoto (1994). The 1989 Macquarie Ridge earthquake: Seismic moment estimation from long-period free oscillations, *J. Geophys. Res.* **99,** doi 10.1029/94JB01251.

Kim, A., and D. Dreger (2008). Rupture process of the 2004 Parkfield earthquake from near-fault seismic waveform and geodetic records, *J. Geophys. Res.* **113,** no. B7, B07308, doi 10.1029/2007JB005115.

Kogan, M. G., W-Y. Kim, Y. Bock, and A. W. Smyth (2008). Load response on the Verrazano Narrows Bridge during the NYC Marathon revealed by GPS and accelerometers, *Seismol. Res. Lett.* **79,** 12–19.

Kouba, J., and P. Heroux (2001). Precise point positioning using IGS orbit and orbit products, *J. Geodes.* **83,** 199–208.

Langbein, J., and Y. Bock (2004). High-rate real-time GPS network at Parkfield: Utility for detecting fault slip and seismic displacements, *Geophys. Res. Lett.* **31,** doi 10.1029/2003GL019408.

Larson, K., P. Bodin, and J. Gomberg (2003). Using 1-Hz GPS data to measure deformations caused by the Denali fault earthquake, *Science* **300,** 1421–1424.

Lee, V. W., and M. D. Trifunac (2009). Empirical scaling of rotational spectra of strong earthquake ground motion, *Bull. Seismol. Soc. Am.* **99,** 1378–1390.

Lewis, F. L., L. Xie, and D. Poppa (2008). *Optimal and Robust Estimation with an Introduction to Stochastic Control Theory*, Second Ed., CRC Press, Boca Raton, Florida, 523 pp.

Mattia, M., M. Rossi, F. Guglielmino, M. Aloisi, and Y. Bock (2004). The shallow plumbing system of Stromboli Island as imaged from 1 Hz instantaneous GPS positions, *Geophys. Res. Lett.* **31,** doi 10.1029/ 2004GL021281.

Maybeck, P. S. (1970). *Stochastic Models, Estimation and Control*, First Ed., Volume **1**, Academic Press, New York, 423 pp.

Miyazaki, S., H. Tsuji, Y. Hatanaka, and T. Tada (1998). The nationwide GPS array as an earth observation system, *Bull. Geogr. Surv. Inst.* **44,** 11–22.

Miyazaki, S, K. M. Larson, K. Choi, K. Hikima, K. Koketsu, P. Bodin, J. Haase, G. Emore, and A. Yamagiwa (2004). Modeling the rupture process of the 2003 September 25 Tokachi-Oki (Hokkaido) earthquake using 1-Hz GPS data, *Geophys. Res. Lett.* **31,** L21603. doi 10.1029/ 2004GL021457.

Moaveni, B., X. He, J. P. Conte, J. I. Restrepo, and M. Panagiotou (2010). System identification study of a 7-story full-scale building slice tested on the UCSD-NEES shake table, *J. Struct. Eng.* **137,** doi 10.1061/ (ASCE)ST.1943-541X.0000300.

Nikolaidis, R, Y. Bock, P. J. de Jonge, P. Shearer, D. C. Agnew, and M. Van Domselaar (2001). Seismic wave observations with the Global Positioning System, *J. Geophys. Res.* **106,** 21,897–21,916.

Panagiotou, M. (2008). Seismic design, testing and analysis of reinforced concrete wall buildings, *Ph.D. Thesis*, University of California, San Diego, California.

Park, J., T.-R. Song, J. Tromp, E. Okal, S. Stein, G. Roult, E. Clevede, G. Laske, H. Kanamori, P. Davis, J. Berger, C. Braitenberg, M. Van Camp, X. Lei, H. Sun, H. Xu, and S. Rosat (2005). Earth's free oscillations excited by the 26 December 2004 Sumatra–Andaman earthquake, *Science* **308,** 1139–1144.

Prawirodirdjo, L., R. McCaffrey, C. D. Chadwell, Y. Bock, and C. Subarya (2010). Geodetic observations of an earthquake cycle at the Sumatra subduction zone: Role of interseismic strain segmentation, *J. Geophys. Res.* **115,** B03414, doi 10.1029/2008JB006139.

Rauch, H. E., F. Tung, and C. T. Striebel (1965). Maximum likelihood estimates of linear dynamic systems, *AIAA J.* **3,** 1445–1450.

Rolandone, F., D. Dreger, M. Murray, and R. Bürgmann (2006). Coseismic slip distribution of the 2003 M_w 6.6 San Simeon earthquake, California, determined from GPS measurements and seismic wave-form data, *Geophys. Res. Lett.* **33,** L16315, doi 10.1029/ 2006GL027079.

Schaffrin, B., and Y. Bock (1988). A unified scheme for processing GPS dual-band observations, *Bull. Géodesique.* **62,** 142–160.

Shakal, A. F., and C. D. Petersen (2001). Acceleration offsets in some FBA's during earthquake shaking, *Seismol. Res. Lett.* **72,** 233.

Smyth, A., and M. Wu (2006). Multi-rate Kalman filtering for the data fusion of displacement and acceleration response measurements in dynamic system monitoring, *Mech. Syst. Signal Process.* **21,** 706–723.

Trifunac, M. D., and M. I. Todorovska (2001). A note on the usable dynamic range of accelerographs recording translation, *Soil Dyn. Earthq. Eng.* **21,** 275–286.

Webb, F., Y. Bock, S. Kedar, S. E. Owen, D. Dong, Jamason, P. Fang, M. B. Squibb, B. W. Crowell, and D. Avraham (2009). Solid earth science data system for exploration of lithospheric deformation in the western U.S., *Eos Trans. AGU* **90,** no. 52, Fall Meet. Suppl., Abstract IN42A-07.

Zumberge, J. F., M. B. Heflin, D. C. Jefferson, and M. M. Watkins (1997). Precise point positioning for the efficient and robust analysis of GPS data from large networks, *J. Geophys. Res.* **102,** 5005–5017.

Cecil H. and Ida M. Green Institute of Geophysics and Planetary Physics
Scripps Institution of Oceanography
9500 Gilman Drive
La Jolla, California 92093-0225
ybock@ucsd.edu